Processes controlling surface, bottom and lateral melt of Arctic sea ice in a state of the art sea ice model

Article

Accepted Version

[1]Centre for Polar Observation and Modelling, Department of Meteorology, University of Reading, Reading, UK.

[2]Centre for Polar Observation and Modelling, Department of Earth Sciences, University College London, London, UK.

[3]Earth System Science Interdisciplinary Center, University of Maryland, College Park, MD, USA

Climate Model, Sea ice, Arctic

Sea ice model, Melt, Processes

Michel Tsamados

m.tsamados@ucl.ac.uk

ABSTRACT

We present a modelling study of processes controlling the summer melt of the Arctic sea ice cover. We perform a sensitivity study and focus our interest on the thermodynamics at the ice-atmosphere and ice-ocean interfaces. We use the Los Alamos community sea ice model CICE, and additionally implement and test three new parameterization schemes: (i) a prognostic mixed layer; (ii) a three equation boundary condition for the salt and heat flux at the ice-ocean interface; and (iii) a new lateral melt parameterization. Recent additions to the CICE model are also tested, including explicit melt ponds, a form drag parameterization, and a halodynamic brine drainage scheme.

The various sea ice parameterizations tested in this sensitivity study introduce a wide spread in the simulated sea ice characteristics. For each simulation, the total melt is decomposed into its surface, bottom and lateral melt components to assess the processes driving melt and how this varies regionally and temporally. Because this study quantifies the relative importance of several processes in driving the summer melt of sea ice, this work can serve as a guide for future research priorities.

Processes controlling surface, bottom and lateral melt of Arctic sea ice in a state of the art sea ice model

Michel Tsamados[1,2], Daniel Feltham[1], Alek Petty[3],

David Schroeder[1] and Daniela Flocco[1]

April 12, 2016

1. Introduction

The Arctic sea ice cover has undergone a rapid decrease in extent (e.g. Stroeve et al. 2012) and thickness (Kwok et al. 2009; Laxon et al. 2013; Lindsay and Schweiger 2015) over recent decades; transitioning from a predominantly multi-year ice pack to an increasingly seasonal ice pack (e.g. Comiso 2011). This decline has been accompanied by increases in sea ice drift (Rampal et al. 2009; Spreen et al. 2011) and deformation (Rampal et al. 2011) over a similar time period. The drastic regime shift observed in recent years suggests that the sea ice models developed following the early field campaigns of the 1960s/1970s (Arctic Ice Dynamics Joint Experiment, AIDJEX), and the 1990s (Surface Heat Budget of the Arctic Ocean, SHEBA) need to be re-evaluated against current sea ice conditions (Notz 2012). Some of the assumptions in these early models have since been challenged, both in their thermodynamic (Feltham et al. 2006; McPhee 2012) and dynamic (Coon et al. 2007; Feltham 2008) components. In this study we seek to understand the processes controlling the summer melt of Arctic sea ice, and thus we focus our attention on the various thermodynamic parameterization schemes included in a state of the art sea ice model.

Large regional and temporal variability in the sea ice state and the oceanic/atmospheric forcing provides a significant challenge when trying to assess the various processes that contribute to Arctic sea ice melt. In addition, *in-situ* measurements that provide a decomposition of sea ice melt processes (top, bottom and lateral melt) are sparse (Richter-Menge et al. 2006; Toole et al. 2011). Recently, (Perovich et al. 2014) quantified the relative importance of surface ice/snow melt and bottom ice melt using autonomous Ice Mass Balance buoys (IMB) deployed over more than ten years (2000 to 2013) that drifted from the North Pole towards the Fram Strait. The study found surface and bottom melt to be of a similar magnitude on average, although both exhibited large inter-annual and regional variability. The study also demonstrated an almost doubling of bottom melt over the period 2008 to 2013 with respect to the period 2000 to 2005. Measurements of lateral melt are lacking and parameterizations of lateral melt in sea ice models are based on observations taken in the 1980s (e.g. Steele (1992) and references therein). The contribution to total Arctic sea ice melt from lateral melt is thought to be small in comparison to bottom and surface melt over high concentration areas, meaning its impact is mainly limited to the marginal ice zone. The increased areal coverage of the summertime marginal ice zone over recent years (Strong et al. 2013) could, however, be increasing the relative importance of lateral melt on a basin scale.

Sensitivity studies of one dimensional models of sea ice have been used in the past to assess the relative importance of different processes in driving the sea ice response to a prescribed external forcing in the Arctic (Ebert and Curry 1993) and in the Antarctic (Petty et al. 2012). These approaches are helpful in understanding the mean behaviour of the sea ice system but fail to capture the spatio-temporal complexity of the sea ice response and ignore feedbacks between the atmosphere, ice and ocean. At the other end of the complexity spectrum, ice-ocean (IO) coupled models (Johnson et al. 2007) and fully coupled atmosphere-ice-ocean (AIO) models (Maslowski et al. 2012; Keen et al. 2013; Rae et al. 2014), can resolve the regional and temporal sea ice response and feedback processes but are computationally expensive and often remain too simplified in representing the physics of

sea ice. As a compromise between physical complexity and computational expense, we use a stand-alone sea ice model coupled to a prognostic ocean mixed layer (denoted ML hereafter) model to quantify the impact of various new physical processes on the sea ice system while retaining realistic regional information.

The total volume of sea ice within the Arctic basin is controlled by a balance between a thermodynamic (growth/melt) and a dynamic (ice import/export) contribution (Hibler et al. 2006). Locally, the sea ice thickness is controlled by the balance of heat conduction ($F_{condbot}$, $F_{condtop}$, see figure 1) and incoming fluxes (F_{ice}, F_{surf}, see figure 1) at its upper and lower surfaces. As illustrated by simple one-dimensional models (Ebert and Curry 1993), the mean sea ice thickness (and by extension the total volume of ice) is sensitive to the external forcing (e.g. temperature, humidity, wind, incoming radiation, ocean heat flux) as well as to the parameterizations used to describe the sea ice thermodynamic processes (e.g. albedo scheme, lead opening, snow and ice thermal properties, treatment of the interfaces). In our stand-alone setup, the external forcing is to a large degree constrained by the reanalysis. However, the use of a prognostic melt pond scheme (Flocco et al. (2012)) modifies the incoming shortwave radiation at the ice-atmosphere interface and the inclusion of the Petty et al. (2014) prognostic ML model alters the basal ice-ocean flux and allows feedbacks between the ice and the ML. Therefore, even with prescribed boundary conditions and a stand-alone sea ice model, the heat budget of the Arctic sea ice (figure 2 a) and ML (figure 2 b) can be substantially modified by the choice of parameterization schemes used.

To better understand the physical mechanisms affecting the large scale retreat of the summer Arctic sea ice cover and the relative importance of lateral melt, basal melt and surface melt, we perform in this paper a sensitivity study of the summer sea ice state and melt to different sea ice physics parameterization schemes. The various model runs are analysed both in terms of their local response to a prescribed external forcing (melt rates, interface temperature, salinity and fluxes) as well as their basin scale ice state characteristics (total extent, area and volume).

The paper is structured as follows: section 2 presents the model setup, the sensitivity studies and the various physical processes assessed in this study; section 3 discusses the model results, the impact on the sea ice state characteristics, the mixed layer properties, and the relative importance of top, bottom and lateral melt in the model; and finally, a discussion and concluding remarks are given in section 4.

2. Processes controlling ice melt in a sea ice model

a. Choice of model configuration

We use version 5.0.2 of the Los Alamos sea ice model, CICE, described in detail by Hunke et al. (2013). This state of the art sea ice model includes a large number of physical parameterization schemes that can be turned on or off by the user. Here we briefly describe the schemes tested in this study.

The model uses multiple ice-thickness categories compatible with the ice thickness redistribution scheme of Lipscomb et al. (2007). We set the number of ice thicknesses to 5 and set the mean ridge height (a tunable parameter) to $\mu_{rdg} = 4$ m$^{1/2}$ (Hunke et al. 2013). We also use the default incremental remapping advection scheme of Lipscomb and Hunke (2004).

In all model runs we choose the elastic-anisotropic-plastic (EAP) rheology described in Tsamados et al. (2013). This rheology is the default choice in our developmental branch of CICE and was shown to result in large regional differences in ice thickness with respect to the default elastic-viscous-plastic (EVP) rheology of Hunke and Dukowicz (2002). We choose the ice strength formulation of Rothrock (1975) and set the empirical parameter that accounts for frictional energy dissipation to $C_f = 17$.

CICE contains three explicit melt pond parameterizations (Hunke et al. 2013) that are used in conjunction with the Delta-Eddington radiation scheme (Briegleb and Light 2007). In all our runs we use the physically based melt pond model of Flocco et al. (2012) which simulates the evolution of melt ponds based on sea ice conditions and external forcing.

In this latest version of CICE, the vertical temperature and salinity profiles as well as the brine volume are calculated. We choose to resolve five ice layers and one snow layer vertically and compare model results between the fixed salinity profile parameterization of Bitz and Lipscomb (1999) and the newly available mushy parameterization, in which the salinity within the ice can evolve in time (halodynamic model of Turner et al. (2013)). The differences between the two models as well as the impact of both halodynamic components on the main sea ice characteristics are discussed in details in Turner and Hunke (2015).

At the ice-ocean interface, we use the ocean heat flux formulation of Maykut and McPhee (1995), $F_{ice} = \rho_w c_p \alpha_h u_* \Delta T$, ρ_w the water density, c_p the specific heat for seawater near freezing and α_h the Stanton number or sensible heat transfer coefficient. The friction velocity is calculated as $u_* = \sqrt{\tau_w/\rho_w}$, where τ_w is the ice-ocean drag (including form drag when calculated (Tsamados et al. 2014)). Finally the temperature difference is taken as $\Delta T = T_{mix} - T_0$, with T_{mix} the mixed layer temperature and T_0 the temperature at the ice-ocean interface. As a default in CICE, T_0 is chosen equal to the freezing temperature of water at the salinity of the mixed layer, $T_0 = T_F(S_{mix})$.

In the default CICE setup both atmospheric (ANDC) and oceanic (ONDC) neutral drag coefficients are assumed constant in time and space. Following Tsamados et al. (2014) and based on recent theoretical developments (Lu et al. 2011; Lüpkes et al. 2012) the total neutral drag coefficients can now be estimated from properties of the ice cover such as ice concentration, vertical extent and area of the ridges, freeboard and floe draft, and size of floes and melt ponds. The new parameterization allows the drag coefficients to be coupled to the sea ice state and therefore to evolve spatially and temporally. For more detail on the implementation we refer the reader to Tsamados et al. (2014). Note that in contrast to the earlier implementations of form drag in Tsamados et al. (2014) or Hunke (2014) we set the Stanton coefficient, α_h, to be proportional to the oceanic neutral drag coefficient, C_{dw}.

As a default setting we choose $\alpha_h = C_{dw}/2$, to be consistent with airborne measurements of neutral drag coefficients for heat and momentum over the Arctic sea ice (see for example

Schröder et al. (2003), Figure 6 b). Note that during the melt season when false bottoms (or any accumulation of low salinity water at the ice-ocean interface) cover a sufficiently large portion of the pack ice and limit bottom heat flux, reducing the parameter α_h can be qualitatively justified. As a simple representation of false bottoms, we therefore modify the ice-ocean heat transfer coefficient according to the melt pond concentration at the ice surface.

For lateral melt we use the parameterization of Maykut and Perovich (1987) and Steele (1992) as implemented in CICE

$$\frac{\partial A}{\partial t} = -w_{lat}\frac{\pi}{\alpha L}A, \tag{1}$$

where A is the sea ice concentration, L is the typical floe diameter (set as a default in CICE to $L = 300$ m), α is a geometrical parameter, and w_{lat} is the lateral melting rate, parameterized as in Perovich (1983), $w_{lat} = m_1 \Delta T^{m_2}$ ($m_1 = 1.6$, $m_2 = 1.36$).

We now describe the implementations that are currently unique to our developmental branch of CICE.

b. Additional processes implemented in this study

(i) Prognostic mixed layer model in the Arctic

The default stand-alone configuration in CICE uses a fixed slab ocean mixed layer (ML) with a prognostic ML temperature, T_{mix}, but a prescribed ML salinity from climatology, S_{mix}, and a constant ML depth, $h_{mix} = 20$ m. Here we include the bulk ML model of Petty et al. (2014) that was used to investigate shelf water formation around Antarctica. This simple prognostic mixed layer model allows the temperature but also the salinity and the depth of the ML to evolve under the influence of surface and deep-ocean heat/salt fluxes. The model is based on the turbulent energy budget approach of Kraus and Turner (1967), which assumes that temperature and salinity are uniform throughout the mixed layer, and

that there is a full balance in the sources and sinks of turbulent kinetic energy. The ML entrainment rate is then calculated by balancing the power needed to entrain water from below with the power provided by the wind and the surface buoyancy fluxes (see Petty et al. (2014) for further details about this model choice).

At the surface the mixed layer receives a heat flux from the ice ($F_{ice} + F_{swthru}$, figure 1) and open-ocean fractions ($F_{s/w}$, figure 1) (all fluxes are positive downwards) and a salt flux calculated in CICE as a combination of ice/snow growth/melt (F^S_{ice}, figure 1) and precipitation and evaporation (F^S_{pe}, figure 1) (note that the rainfall and melt water on sea ice is assumed to percolate through the sea ice and enters the ML). In the winter as the ML deepens, heat and salt from the ocean below at the temperature, T_b, and salinity, S_b, are entrained in the ML (respectively fluxes, F_{bot} and F^S_{bot}, figure 1), while in the summer as the ML shallows and leaves behind a layer of Winter Water there are no heat or salt fluxes at the bottom of the ML. In our implementation we introduce a minimum ML depth, h^{min}_{mix}, and assume that there are no heat and salt exchanges between the ML and the ocean below when the ML reaches this minimum.

We apply a slow ($\tau_r = 20$ days) temperature restoring of the ML temperature towards a monthly climatology of the 10 m depth reanalysis temperature taken from MYO-WP4-PUM-GLOBAL-REANALYSIS-PHYS-001-004 reanalysis (Ferry et al. 2011) (hereafter noted MYO). This temperature restoring can be seen as a parameterization of the advection of heat in the upper ocean. The weak temperature restoring is consistent with model results from a coupled ice-ocean model (Steele et al. 2010) that found in the Arctic advection under the pack ice to be relatively small in comparison with surface heat fluxes. To represent oceanic heat flux convergence melting sea ice at the ice edge (Bitz et al. 2006), we adopt a faster temperature restoring (τ_r=2 days) when $T_{mix} > T^{MYO}_{mix} + 0.2$. Note that the value of 0.2° C is large enough to ensure that the fast restoring mainly occurs in the winter around the ice edge. This ad-hoc method is equivalent to applying an additional heat flux to the ML, $F_{adv} = (T_{mix} - T^{MYO}_{mix})/(\tau_r \rho_w c_p h_{mix})$ (see figure 1 a). The fast temperature restoring is mostly

important in controlling the winter sea ice extent while the slow temperature restoring acts as a heat sink for the ML in the summer.

In addition to this temperature restoring we use a slow (365 days) restoring to the sea surface salinity in the ML. In our new prognostic ML setup the freezing temperature of the mixed layer is updated to account for the modified salinity of the ML. As the ML shallows at the onset of melt, Winter Water is left behind in the deep ocean grid. The deep ocean salinity and temperature are then slowly restored with a time scale of 1 year to a winter (January 1st) climatology (1993-2010) from the MYO reanalysis. The ocean properties below the mixed layer are therefore relaxed towards observed climatology; isolating the effect of surface forcing and allowing us to understand short term (seasonal) variations in the ML.

(ii) Lateral melting and floe size distribution

We generalize the lateral melt parameterization of equation (1) to account for a power law distribution of floe sizes, in order to be consistent with observations (e.g. Herman (2010) and references therein). In our new lateral melt parameterization scheme, the variable L in equation (1) represents the average floe size instead of representing a unique floe size as in the default lateral melt scheme.

For typical winter pack ice $L \geq 100$ m (Weiss and Marsan 2004) and lateral melting is negligible in comparison to bottom and surface melting (Steele et al. 1989). In summer, the average floe size decreases and the relative importance of lateral melting to basal melting increases as the ratio of perimeter to area increases. Wave-ice interaction fractures the ice and leads to smaller floes in the marginal ice zone. The average floe size typically varies with the ice concentration and was parameterized in the marginal ice zone by Lüpkes et al. (2012) to be:

$$L = L_{min} \left(\frac{A_\star}{A_\star - A} \right)^\beta , \tag{2}$$

where $A_\star$ is introduced instead of the value 1 to avoid a singularity at $A = 1$, the exponent β

is chosen in the range 0.2 to 1.4 ($\beta = 0.5$ in this study), and L_{min} is a characteristic minimal floe size ($L_{min} = 8$m in this study). Here, we have extended this parameterization to the entire ice cover, but note that in the case where $L \geq 100$ m the contribution from lateral melting becomes negligible and the floe size parameterization becomes irrelevant to lateral melt.

In the appendix we show that if one uses a power law floe size distribution, then the total lateral melt is reduced relatively to the situation with a unique floe size. Lateral melt is reduced by a factor $P_0(\zeta)$ applied to the right hand side of equation (1),

$$\frac{\partial A}{\partial t} = -P_0(\zeta) w_{lat} \frac{\pi}{\alpha L} A, \tag{3}$$

where ζ is the power exponent of the power law distribution $n_r(r)$, with $\frac{n_r(r)}{\pi r^2}$, being the number of floes of size r per unit area. Typical observed values of ζ are in the range 1 to 2 with the corresponding values of the attenuation pre-factor, respectively $P_0(1) = 0$ and $P_0(2) = 0.75$. In this study we choose $\zeta = 1.13$ and $P_0(1.13) = 0.2$. We should note that the choice of the exponent ζ is subjective and needs to be constrained further from observations.

(iii) Three equation boundary conditions

The Maykut and McPhee (1995) formulation of the heat flux from the ocean into the ice, F_{ice} (see section 2a), depends on the interfacial temperature, T_0. As discussed in Schmidt et al. (2004), the interfacial temperature can be chosen in models as: (i) a constant freezing temperature of sea water (typically sea water at a salinity of 34 PSU); (ii) the freezing temperature of the ML (default option in CICE); or (iii) the freezing temperature, T_f, of the sea water directly below the sea ice with the interfacial salinity, S_0, that in the summer can be fresher than the water in the ML due to the freshwater fluxes associated with melting. In this latter case one must solve the following system of three equations described in Notz (2005) and McPhee (2008):

$$- F_{condbot} + \rho_w c_p \alpha_h u_0^* \left(T_{mix} - T_0\right) - q\dot{h}_0 = 0, \tag{4}$$

$$\alpha_s u_0^* \left(S_{mix} - S_0\right) + \dot{h}_0 \left(S_{ice} - S_0\right) = 0, \tag{5}$$

$$T_0 = T_f(S_0) \simeq -mS_0, \tag{6}$$

where $F_{condbot}$ is the downward ice conductive heat flux at the basal surface, q is the enthalpy of new ice forming with the salinity and freezing temperature of the sea surface and $\dot{h}_0$ is the rate of ice growth at the ice-ocean interface. T_{mix} and S_{mix} are respectively the temperature and salinity of the mixed layer. The exchange coefficients for salinity and heat are different under melting conditions, $\alpha_s = \alpha_h/50$ and under freezing conditions, $\alpha_s = \alpha_h$ (McPhee 2008).

Note that this is a new parameterization scheme included in CICE. We solve the system of equations (4)-(6) separately for each ice thickness category and save T_0, S_0 as well as all fluxes as output variables. Note that this parameterization scheme is only operational in CICE when the mushy layer parameterization of Turner et al. (2013) is switched on.

c. Reference model run and sensitivity model runs

We describe in this section our chosen reference run and model sensitivity runs. Our ambition is not to find an optimal model configuration but instead to test the impact of the model physics on a sufficiently realistic model configuration. The reference configuration follows largely from previous work by Tsamados et al. (2014) and Schröder et al. (2014) that included several recent model developments (see section 2a) and was able to demonstrate good agreement to the observed September sea ice extent. In addition our reference model configuration was chosen to reproduce reasonably well the main sea ice characteristics in the summer months, in particular the sea ice concentration in August that is often underestimated in models (Notz 2013). Because they are implemented in CICE for the first time, we focus in particular in our sensitivity study on the processes described in section 2b.

In the reference run, *REF*, most model implementations described in sections 2a and b are switched on, namely: the prognostic mixed layer of Petty et al. (2014); the three equation boundary condition treatment of the ice-ocean interface; the mushy layer thermodynamic implementation of Turner et al. (2013); the form drag parameterization of Tsamados et al. (2014); a heat transfer coefficient proportional to the oceanic neutral drag coefficient, $\alpha_h = C_{dw}/2$. On the other hand the new lateral melt parameterization is not used.

In addition to the *REF* run we perform a series of sensitivity runs. We adopt for each physical process a simple on-off approach where each additional model run contains a simple modification with respect to the *REF* run. The names and changes in these sensitivity runs are as follows. In *MLD_CST* we use the default fixed depth slab ocean ML described in 2i); in *MLD_MIN_2M* we set the minimum allowed ML depth to $h_{mix} = 2$ m; in *NO_3EQTN* we revert to the default boundary condition treatment with $T_0 = T_f(S_{mix})$ (see 2iii); in *NO_MUSHY* we replace the mushy parameterization and flushing of Turner and Hunke (2015) by the fixed salinity profile scheme of Bitz and Lipscomb (1999) (section 2a); *DBL_ALPHA_H*, *DBL_ALPHA_H / NO_3EQTN* and *DBL_ALPHA_H / NO_MUSHY* are the same as *REF*, *NO_3EQTN* and *NO_MUSHY* but with a doubling of α_h (section 2a); in *NO_POND* we artificially set the thickness of the melt ponds to zero; in *FALSE_BOTTOM* to simply model the impact of under ice fresh water accumulation on the bottom heat flux we double α_h where melt ponds cover more than 20% of the ice surface; in *NO_FORM_DRAG* we switch off the Tsamados et al. (2014) form drag parameterization (section 2a); in *LAT_MELT* we switch on the lateral melt parameterization described in section 2b; finally in *SST_TIME* we restore the sea surface temperature to the time dependent temperature of the MYO reanalysis surface ocean temperature over the period 1993 to 2010 (because the ocean reanalysis is limited to this period). All the sensitivity runs are summarized in table 1.

All simulations are run in stand-alone mode on a 1° tripolar (129×104) grid that covers the whole Arctic Ocean (note that the Hudson Bay and part of the Canadian Archipeleago are treated as land) with a horizontal grid resolution of around 50 km. Atmospheric forcing

data are taken from the NCEP-NCAR reanalysis (Kanamitsu et al. 2002): 6-hourly 10-m winds, 2-m temperatures and 2-m humidity, daily shortwave and longwave radiation as well as monthly snowfall and precipitation rates. Sea surface temperature (SST) and salinity (SSS) are taken from the MYO reanalysis (Ferry et al. 2011) to initialize the Arctic sea ice state. Climatological monthly means from Ferry et al. (2011) are used for the ocean currents (depth of 10 m). Starting with an homogeneous sea ice with thickness of 2.5 m, a snow depth of 20 cm and a concentration of 100% the reference model, REF, is spun up for 10 years (1980-1989) once. This configuration is used as initial condition for all the simulation runs described in table 1 that are then run for a period of 24 years (1990-2013).

3. Results of a sensitivity study

a. Relative importance of top, bottom and lateral melt

In this section we describe the impact of the various parameterization schemes on the summer Arctic sea ice-mixed layer state. Figure 3 shows the mean seasonal and inter-annual mixed layer temperature T_{mix} (figure 3 a and b), mixed layer salinity S_{mix} (figure 3 e and f), and mixed layer depth h_{mix} (figure 3 i and j) for each model simulation. To decompose the thermodynamic response of each model simulation and to quantify the relative importance of top, bottom and lateral melt, figure 3 shows the mean seasonal and inter-annual surface melt rate (figure 3 c and d), bottom melt rate (figure 3 g and h) and lateral melt rate (figure 3 k and l).

Looking first at the mean upper ocean characteristics, we see that the seasonal cycle of h_{mix} is important in controlling the temperature and salinity of the ML. From a simple heat and salt conservation argument (equations 14 and 15 in Petty et al. (2014)) the shallowing of the ML in the summer season results in an increase of the average T_{mix} (figure 3 a), from an average maximum in July of $\sim -1.0^{\circ}$ C in *MLD_CST* to $\sim -0.8^{\circ}$C in *REF* and $\sim -0.5^{\circ}$C in *MLD_MIN_2M* and a reduction of the average minimum SSS in July (figure 3 e) from

$\sim$ 31.3 PSU to $\sim$ 29 PSU and $\sim$ 27.4 PSU. In addition to the seasonal dependence the ML appears to be warming (figure 3 b) and freshening (figure 3 f) over the last 2 decades in July and this trend is stronger for the shallower summer ML in *MLD_MIN_2M*. Interestingly, despite having a thicker h_{mix}, *NO_MUSHY* displays very similar T_{mix} characteristics as in *MLD_MIN_2M*. This reflects the additional incoming solar radiation in this model run that was shown by Turner and Hunke (2015) to be related to the reduced flushing rate in the Bitz and Lipscomb (1999) parameterization resulting in a larger pond area fraction and a lower albedo. The summer T_{mix} climatology in *NO_3EQTN*, *NO_FORM_DRAG*, *NO_POND* and *SST_TIME* is lower than *REF* by approximately 0.1°C. Note also that in *SST_TIME* there is a strong warming trend of the ML and the interannual variability of T_{mix} is much larger than in *REF*. This points to the importance of the oceanic temperature restoring scheme used in a stand-alone setting. These variations in the mean ML characteristics can help us explain the differing bottom and lateral melt rates from each simulation as discussed next.

The bottom and lateral heat fluxes scale respectively with ΔT and ΔT^{m_2} ($\Delta T = T_{mix} - T_0$, see section 2c). Intuitively one might therefore expect a higher summer T_{mix} will contribute to an increase in the bottom and lateral heat flux. However, a fresher ML results in an increased freezing temperature at the ice-ocean interface (here we assume $T_0 = T_F(S_{mix})$) which will reduce the bottom and lateral heat flux. Comparing *MLD_CST* and *REF* in figure 3 g and h, we can see that despite the higher T_{mix} in the REF simulation, the impact on the average local bottom melt is negligible. In the *MLD_MIN_2M* and *NO_MUSHY* simulations, however, the increase in T_{mix} compared to *REF* appears sufficient to cause a significant increase in the bottom and lateral melt (see figure 3 h and l). Finally, the *NO_3EQTN* simulation demonstrates the insulating effect caused by switching on the three equation boundary conditions. Indeed despite the higher T_{mix} throughout summer in the *REF* simulation, the bottom melt rate is significantly higher on average for *NO_3EQTN*. This can only be explained by the larger interfacial temperature in *REF* (not shown) that, in contrast to *NO_3EQTN*, is taken as the freezing temperature of the fresher water directly

below the sea ice (see equations (4)-(6)).

The mean seasonal (figure 3 (c), (g) and (k)) and annual time-series (figure 3 (d), (h) and (l)) of the basin average surface, bottom and lateral melt rates show that the bottom melt is the strongest contributor to the total melt (up to ~ 1.5 cm/day in July for *REF*). The top melt is the second strongest contribution (up to ~ 1.25 cm/day in July for *REF*) and, as expected, is largely insensitive to modifications to the ML. Except in the case of the floe size dependent lateral melt parameterization, *LAT_MELT*, the contribution from lateral melt is on average small (up to ~ 0.25 cm/day in July for *REF*). For the *REF* simulation in July, surface melt shows the highest interannual variability, with a standard deviation of 0.41 cm/day (figure 3 d), compared with 0.29 cm/day for bottom melt (figure 3 h) and 0.06 cm/day for lateral melt (figure 3 l). These results suggest that in our model implementation, interannual variability of the summer sea ice characteristics (area, extent, volume) will be dominated by the surface melt processes. This could explain why the inclusion of a realistic description of surface melt ponds in CICE results in significant skill in reproducing and forecasting the September sea ice extent (Schröder et al. 2014). Note also that the lower interannual variability in *REF* (0.29 cm/day) compared to *SST_TIME* (0.36 cm/day) could indicate that the simulations without temperature restoring to a time dependent reanalysis might underestimate the true variability of the upper ocean temperature and salinity.

Figure 4 decomposes the changes in the total volume of ice into its various thermodynamic components during ice growth (congelation growth, frazil ice formation and snow ice formation) and ice melt (surface melt, bottom melt and lateral melt). Figure 4 shows that the mean annual ice growth is dominated in all sensitivity simulations by congelation growth ($+9500\text{km}^3$ in *REF*), followed by frazil ice formation ($+4100\text{km}^3$ in *REF*), and snow ice formation ($+800\text{km}^3$ in *REF*). The mean annual ice melt is dominated by bottom melt (-10000km^3 in *REF*), followed by surface melt (-3200km^3 in *REF*) and lateral melt (-1200km^3 in *REF*). In all the simulations, the total annual ice melt and growth largely cancel each other out over the full annual cycle, leaving only a small negative term

associated with the expected ice volume decline over the 1993 to 2010 period. The differences in the mean total sea ice volume across all simulations occurs in a transient period of up to five years from 1990 to 1994 (not shown). Three simulations stand out in figure 4, *NO_MUSHY*, *LAT_MELT* and *SST_TIME*. Relative to *REF*, *NO_MUSHY* shows an overall increase in congelation growth ($+3750\text{km}^3$) and a reduction in surface melt (-900km^3) and lateral melt (-200km^3), compensated by a decrease in frazil ice formation (-3100km^3) and an increase in snow ice formation ($+850\text{km}^3$) and bottom melt ($+950\text{km}^3$). The increase in lateral melt in *LAT_MELT* (-2500km^3) is largely compensated by a reduction in bottom melt ($+2200\text{km}^3$) reflecting the fact that the heat available in the ML to melt the ice from below is divided between lateral and bottom melt. In *SST_TIME*, a large increase in frazil ice formation is compensated by less congelation growth and increased bottom melt. These compensating effects are examples of the negative feedback processes that take place during the thermodynamic cycle of sea ice.

Decomposing the total ice melt shows that bottom melt accounts for more than two thirds of the total ice melt, top melt accounts for almost a third of the total and lateral melt contributes less than 10%. Looking at the ice melt across individual months (not shown) shows that a significant fraction of the total bottom melt occurs outside the summer melt season (from September to April), featuring monthly ice melt volumes of -2000km^3 to -5000km^3. Over the same monthly time period, the contribution to the total melt from surface and lateral melt is small. Looking at maps of ice melt (similar to figure 6) for the September to April months (not shown) demonstrates that this 'winter' bottom melt contribution occurs mainly around the ice edge, driven by warm southern Atlantic and Pacific waters. In the *REF* simulation, the monthly (inter-annual) mean ice melt in June, July and August is -6000km^3, -28000km^3 and -5000km^3 for surface melt, -22000km^3, -38000km^3 and -22000km^3 for bottom melt and -4000km^3, -5000km^3 and -3000km^3 for lateral melt.

We now look at the spatial pattern of the surface (figure 5), bottom (figure 6) and lateral

(figure 7) melt for each simulation for July (the maximum melt month). In these figures, absolute melt rates are shown for *REF*, while relative values are shown for all other model runs. Looking first at the absolute values of the melt rates in *REF* we see that the mean July surface melt rate is high (~ 1.5 cm/day) over most of the Arctic basin and is low (< 0.5 cm/day) over the Fram Strait, the ice edge and the region of thicker ice north of Greenland and the Canadian Archipelago. Note that the regions of increased surface melt correspond to regions of larger than average pond coverage (not shown). The bottom and lateral melt rates are higher (≥ 1.5 cm/day and ≥ 0.25 cm/day respectively) in regions of low concentration ($A < 80\%$), where solar radiation can penetrate the upper ocean and increase the mixed layer temperature.

Figure 5 shows that model runs using the Bitz and Lipscomb (1999) parameterization for salinity and flushing (*NO_MUSHY*, *DBL_ALPHA_H / NO_MUSHY* and *FALSE_BOTTOM*) result in a large increase in surface melt (+0.25 cm/day to +0.5cm/day). This is the result of a slower flushing of melt ponds resulting in a lower surface albedo and higher incoming solar radiation. This in-turn leads to increased heat transfer to the mixed layer and an increase bottom (+0.25 cm/day to +1.0cm/day) and lateral melt rate (up to +0.1 cm/day) over most of the Arctic Ocean. The similarity in the spatial patterns of bottom and lateral melt *DBL_ALPHA_H / NO_MUSHY* and *FALSE_BOTTOM* demonstrates that reducing the heat transfer coefficient only in those location that present large coverage of ponds (pond area larger than 20%) is sufficient to significantly reduce the oceanic melt. This hints to the potentially important role of under ice melt ponds and false bottom formation in controlling the sea ice state.

In *LAT_MELT* we observe a large increase of lateral melt over the ice edge (≥ 0.5 cm/day) that is accompanied by a reduction in bottom melt (≤ -0.5 cm/day). This highlights that if more heat is used to melt the ice laterally, less heat is available for bottom melt. Figure 5 shows a decrease in *NO_FORM_DRAG* of bottom melt under heavily ridged ice north of Greenland and the Canadian Archipelago (≤ -0.25 cm/day) that we attribute to a reduction

in *NO_FORM_DRAG* with respect to *REF* of the oceanic drag coefficient, C_{dw}, and hence a reduction in the heat transfer coefficient, $\alpha_h = C_{dw}/2$.

Other interesting spatial features include the near identical spatial patterns of bottom and lateral melt rates in *MLD_CST* and *NO_POND* which mirror the melt rates observed in *MLD_MIN_2M*. We also note that turning off the 3 equation boundary conditions in the *NO_3EQTN* simulation results in an increased bottom and lateral melt in the marginal ice zone. In order to fully understand the pattern of the melt rates discussed above we now look at the impact on the main sea ice and mixed layer characteristics.

b. Regional sea ice and mixed layer patterns

The ice cover is a complex heterogeneous system and in this section we assess how different regions respond to the different physical parameterization schemes. For all model simulations (described in table 1) we calculate for each model grid cell a climatology (over the period 1993 to 2013) of sea ice concentration (A), sea ice thickness (H), ML temperature (T_{mix}) and ML salinity (S_{mix}). As discussed in the introduction, the main focus of this study is in understanding the sensitivity of sea ice melt to various sea ice physics parameterization. Nevertheless, our reference run was chosen to agree qualitatively with ice concentration data obtained from the Special Sensor Microwave Imager (SSM/I) passive microwave radiometer and with ice thickness from the Pan-Arctic Ice Ocean Modeling and Assimilation System (PIOMAS).

Comparing h_{mix} from Ice Tethered Profilers (ITP) measurements (2004-2013) and the MYO reanalysis we find that the simulations presented in this study featuring only a simple prognostic ML model reproduce also qualitatively the shallow and stable ML observed across the Arctic (see also Peralta-Ferriz et al. (2014)). In the summer the *REF* simulation and the MYO reanalysis show a shallower ML depth than the ITP measurements, including a minimum depth of $h_{mix} \sim 10$ m over the entire Arctic Ocean. The *REF* simulation ML depths agree with the ITP measurements in the Beaufort Sea but underestimate the ML

depths in the pack ice north of Greenland. Similar maps of the mixed layer temperature (T_{mix}) and salinity (S_{mix}) (not shown) illustrate the tendency of the *REF* simulation to overestimate (both against ITP and MYO) the heating of the ML in August, which in turn results in additional melt and a lower S_{mix}.

In figures 8 to 11 we show maps of the main sea ice and mixed layer characteristics. We show the absolute values for the reference *REF* simulation and the relative values with respect to *REF* for all other model simulations. We have computed these maps for all months but choose here to only show August. This choice is motivated first by the fact that August has the largest differences between the different sensitivity model runs in our study and also because August sea ice concentration is often underestimated in current sea ice models (Notz 2013).

Comparing first *REF*, *MLD_CST* and *MLD_MIN_2M* we see that switching off the prognostic mixed layer results in a large increase in ice concentration (A$> +10\%$, figure 8) and decrease in the ML temperature ($T_{mix} < -0.4$°C, figure 10) over most of the eastern Arctic Ocean (where $A < 80\%$, figure 8). Reducing the value of the minimum mixed layer depth (to $h_{mix} = 2$ m) has the opposite effect and results in a large decrease in concentration (A$< -10\%$, figure 8) and increase in the ML temperature ($T_{mix} > +0.4$°C) over the same region. The impact on ice thickness is more diffuse, with a homogeneous increase in the mean ice thickness (+10cm-25cm, figure 9) over most of the Arctic basin for *MLD_CST* and a corresponding increase in the mixed layer salinity ($> +2$, figure 11). *MLD_MIN_2M* shows a decrease in ice thickness (-50cm to -100cm) over a similar region to *MLD_CST* and a corresponding decrease of the mixed layer salinity (< -2 PSU). This indicates that to a leading order, the ML temperature tends to evolve with sea ice concentration (due to modified incoming solar radiation) while the ML salinity evolves with ice thickness (due to salt exchanges during ice melt/growth). Note that these results hold also in July and throughout the summer season (not shown).

We now turn to *REF*, *NO_3EQTN* and *NO_MUSHY* (results for *DBL_ALPHA_H*, *DBL_ALPHA_H*

/ *NO_3EQTN* and *DBL_ALPHA_H* / *NO_MUSHY* are qualitatively similar) to quantify the impact of the sea ice salinity dynamics, flushing and three equation boundary condition on the sea ice and ML. Because of the larger incoming solar radiation associated with the default halodynamic model of Bitz and Lipscomb (1999) and the default CICE flushing parameterization, sea ice concentration is reduced in *NO_MUSHY* with respect to *REF* by more than 10%, sea ice thickness is reduced by more than 1m, T_{mix} is lower by more than 0.4°C, and S_{mix} is lower by $0.5-1$ PSU over most of the Arctic Ocean. Note that *FALSE_BOTTOM*, the simulation that uses the same Bitz and Lipscomb (1999) parameterization has a similar low sea ice state bias. Comparing *REF* and *NO_3EQTN*, we see that the differences are smaller ($\Delta A \sim -5\%$, $\Delta H \sim -20$cm, $\Delta T_{mix} \sim +0.3$°C and $\Delta S_{mix} \sim 0$ PSU), the impact is localised over the marginal ice zone and happens almost exclusively in the summer season (June and July not shown). This is consistent with the larger melt rate in this region in *NO_3EQTN* and reflects the fact the 3 equation boundary condition is most effective where there is a source of fresh melted water at the ice-ocean interface, hence lowering the interfacial salinity, S_0, and reducing the bottom heat flux (see equations (4) to (6) in section 2b).

The impact of switching off the form drag parameterization of Tsamados et al. (2014) in *NO_FORM_DRAG* is spatially bi-modal; increasing the summer concentration (marginally), ice thickness ($\Delta H \sim +1$m) and ML salinity ($\Delta S_{mix} \sim 1$ PSU) in the heavily ridged regions north of Greenland and the Canadian Archipelago, and decreasing the ice concentration ($\Delta A \sim -10\%$) and ice thickness ($\Delta H \sim -25$cm) while increasing the ML temperature ($\Delta T_{mix} \sim +0.3$°C) over the Russian continental shelves. As discussed in section 3a, these differences can be largely explained by increased (reduced) interfacial heat fluxes due to the higher (lower) than average atmospheric and oceanic heat exchange coefficients in the former (later) regions when the form drag is accounted for.

Switching off the melt ponds in *NO_POND* results, as expected, in a large increase in the concentration and volume of ice throughout the summer season, due to a lowering of the

incoming solar radiation, F_s. In August, for example, the patterns are similar, albeit more intense, to *MLD_CST* with a large increase of A and decrease of T_{mix} over most of the eastern portion of the Arctic Ocean and a more homogeneous increase of S_{mix} and H. Interestingly *FALSE_BOTTOM* performs very much like *NO_MUSHY* (and less like *DBL_ALPHA_H / NO_MUSHY*), indicating that reducing the bottom heat flux whenever melt ponds are prevalent could play an important role in accurately simulating the total mass balance of the Arctic sea ice cover.

Introducing the new lateral melt parameterization in *LAT_MELT* results in a significant decrease of concentration ($\Delta A \sim -7.5\%$) and thickness ($\Delta H \sim -20$cm) in the marginal ice zone, but without noticeable changes of the mixed layer salinity and temperature.

c. Impact on the main sea ice characteristics

We now assess the main sea ice characteristics from the various model simulations over the entire Arctic basin. This provides a simple overview of the sea ice response to prescribed atmospheric and oceanic forcing. In figure 12, we look at the impact of the new model physics on the total ice area (figure 12 a-c), total ice extent (figure 12 d-f), and total ice volume (figure 12 g-i). To distinguish between the different model responses shown in figure 12 we present in figures 13 (a-c) and 14 (a-c) a series of scatter plots showing the average and trend in sea ice area (SIA), sea ice extent (SIE, defined as the total area covered by ice with a concentration higher than 15%)) and sea ice volume (SIV) over the period 1993 to 2010 in August and September (note that we use the same colour scheme as in figure 12). The slightly shorter time period chosen reflects the time span of the *SST_TIME* simulation that is limited by the MYO reanalysis data used. Note that the results shown on figures 13 and 14 are similar over the period 1993 to 2013.

In order to assess the inter-annual variability of the model simulations, we also calculate the correlation and de-trended correlation between each model run annual time-series (SIA, SIE and SIV) and the corresponding observational dataset. Figures 13 (d-f) and 14 (d-f)

show these results in a scatter plot format respectively in August and September. Note that we choose to compare the SIA and SIE results to the Bootstrap processing of passive microwave data (Comiso 2000). While absolute values between NASA Team and Bootstrap sea ice concentration vary considerably in the summer, the detrended time series are similar. For comparison purposes we also show a point corresponding to the Schröder et al. (2014) model setup that we refer to as *SFFT14*.

Figures 13 and 14 reveal that the physical processes tested in this study introduce a wide spread in the main sea ice characteristics in both the mean and the trend. In September the average SIA ranges from 3.1×10^6 km^2 (*NO_MUSHY*) to 5.1×10^6 km^2 (*SST_TIME*), the average SIE from 4.5×10^6 km^2 (*DBL_ALPHA_H / NO_MUSHY*) to 6.2×10^6 km^2 (*SST_TIME*) and the average SIV from 4.0×10^6 km^2 (*DBL_ALPHA_H / NO_MUSHY*) to 12.7×10^6 km^2 (*SST_TIME*). The September SIA trend ranges from -1700×10^6 km^2/decade (*SST_TIME*) to -750×10^6 km^2/decade (*NO_POND*), the SIE trend ranges from -1400×10^6 km^2/decade (*SFFT14*) to -620×10^6 km^2/decade (*MLD_CST*), and the SIV trend ranges from -3.9×10^{12} m^3 (*SST_TIME*) to -1.6×10^{12} m^3/decade (*DBL_ALPHA_H / NO_MUSHY*).

Looking in more detail at the individual runs in figures 13 a-c and 14 a-c, we see that the average SIA, SIE and SIV (to a lesser degree) of most model simulations are larger than for the *SFFT14* simulation of Schröder et al. (2014) and closer to the passive microwave observations (not closer to PIOMAS). The only simulations that have similar SIA and SIE (but lower SIV) to the *SFFT14* run are *NO_MUSHY* and *DBL_ALPHA_H / NO_MUSHY* that use the same thermodynamic treatment of the ice Bitz and Lipscomb (1999) and the same parameterization of the flushing of melt ponds (Turner and Hunke 2015) as is used in Schröder et al. (2014). Two outlier runs on figure 12, *NO_MUSHY* (and *DBL_ALPHA_H / NO_MUSHY* not shown) and *SST_TIME* (and to a lesser degree *NO_POND*), show a very low and high total volume of ice throughout the season (figures 12 (g-i)). In *SST_TIME* we use a time dependent SST from the MYO reanalysis which is equivalent to modifying the

oceanic flux F_{adv} shown on figure 1. As clearly demonstrated in Turner and Hunke (2015), by introducing a new mushy layer thermodynamic scheme (Turner et al. 2013) (*NO_3EQTN* and *REF*), we also modify the flushing parameterization used in the earlier setup of CICE (Bitz and Lipscomb 1999) (*NO_MUSHY*). This results in less melt pond water being flushed in the summer in *NO_MUSHY* as opposed to in *NO_3EQTN* (or *REF*) which lowers the albedo and increases the incoming shortwave radiation penetrating the sea ice and mixed layer system, resulting in a strong reduction in sea ice volume as shown in figures 12 (g-i). This is also highlighted by the additional ice surface heat flux F_s, in *REF* compared to *NO_MUSHY*. Inversely, in *NO_POND* where the thickness and area of the melt ponds are set artificially to zero, the surface heat flux, F_s, is reduced, resulting in less ice melt and a slower ice edge retreat (see figures 12, 13 and 14).

Observed differences in the mean sea ice characteristics between the various model simulations can also be related to a shift in their seasonal responses. As highlighted in figure 12, introducing a prognostic ML results in an overall depletion of ice across the Arctic (in both thickness and concentration). From figure 12 g (but also a and d) we see that from January to May, the sea ice in the reference run *REF* does grows slower than in *MLD_CST*. We attribute this to the entrainment of warm water from the deeper ocean as the mixed layer deepens from about 30 m in January to about 50 m in May, resulting in a large positive bottom flux F_{bot} (figure 2) that is not present in the *MLD_CST* run. Looking at the mean ice growth and melt contributions in figure 4 and for individual months shows that the difference is due to less frazil ice formation in *REF* between January and May as discussed in section 3a

As expected, the trends in SIV correlate with the mean SIV (see figures 13 c and 14 c). For example, the ice covered area ice in August in *SST_TIME* is almost double that of *NO_MUSHY* and melting sea ice at the same volume per decade in both runs would require a significant increase in the local melt rates that has no physical justification. Hence, the sea ice volume trend is more than halved in *NO_MUSHY* ($-1.7 \times 10^{12}\mathrm{m}^3$/decade in September)

in comparison to *SST_TIME* (-4×10^{12}m^3/decade in September) as shown in figure 14 c.

We turn now to the scatter plot correlations presented in figures 13 d-f and 14 d-f. In the following discussion we denote R the correlation and $R^\star$ the detrended correlation. Figure 13 d-f shows that apart from *SFFT14* and *SST_TIME*, all other runs perform relatively poorly in reproducing the observed variability in the August SIA ($R \leq 0.75$ and $R^\star \leq 0.45$) and only slightly better for the SIE ($R \leq 0.85$ and $R^\star \leq 0.6$) and SIV ($R \leq 0.88$ and $R^\star \leq 0.63$). The September correlations (figures 14 d-f) are higher in all simulations for SIA ($0.86 \leq R \leq 0.95$ and $0.6 \leq R^\star \leq 0.86$) and SIE ($0.82 \leq R \leq 0.95$ and $0.53 \leq R^\star \leq 0.86$) and similar for SIV ($0.86 \leq R \leq 0.92$ and $0.45 \leq R^\star \leq 0.8$). The *SFFT14* and *SST_TIME* runs still perform best across all characteristics but note that *NO_MUSHY*, *DBL_ALPHA_H / NO_MUSHY*, *DBL_ALPHA_H / NO_3EQTN*, FD/OFF and *DBL_ALPHA_H* also perform well (in decreasing order) in representing the observed interannual variability of the SIE.

Summarising figures 12, 13 and 14 one can conclude that introducing the new physical parameterizations schemes described in section 2 and, in particular, the new mushy-layer thermodynamic approach of Turner et al. (2013) can improve the main basin average characteristics of the sea ice with respect to the *SFFT14* setup. The improvement is particularly clear for the August SIA and SIE and the September SIA. However, the potential improvement in simulating the sea ice trends is not so clear, where we see an improvement in the August SIE trend but a deterioration of the SIV trends. The inter-annual variability of the main sea ice characteristics quantified by the correlation coefficients, R and $R^\star$, figures 13 and 14 show that the model simulations (with the exception of *SST*) do not perform as well as the *SFFT14* simulation. To understand these differences one must realise that inter-annual variability is dependent on the mean state of the ice pack. We expect, for example, a thinner and less concentrated sea ice cover to be more responsive to interannual variability in the external forcing. This highlights the fact that even within a stand-alone setup, tuning a sea ice model to reproduce simultaneously the mean, trends and interannual variability of the main sea ice characteristics is a delicate exercise. Interestingly we find that

the *SST_TIME* simulation outperforms all other model runs in almost every single category both in terms of averages and correlations (note that the *SFFT14* run is better at capturing September SIE interannual variability). While this result is unsurprising in the sense that a time dependent sea surface temperature from reanalysis captures a large part of the inter-annual variability of the atmospheric and oceanic forcing as well as of the sea ice extent, it nevertheless highlights once more the importance of the upper ocean in driving the sea ice response and the coupled nature of the sea ice - mixed layer system (Toole et al. 2010; Perovich et al. 2014).

4. Discussion and conclusion

We have presented a stand-alone sea ice model sensitivity study focusing on the processes controlling the summer melt of Arctic sea ice. In addition to the parameterization schemes already implemented in the state of the art Los Alamos community sea ice model CICE, v5.0.2 (e.g. explicit melt ponds, a form drag parameterization, and a halodynamic brine drainage scheme) we implement in the model and test three new schemes: i) a prognostic mixed layer model; ii) a three equation boundary condition; and iii) a parameterization of lateral melting explicitly accounting for the average floe size and floe size distribution dependence. For each simulation, the total melt is decomposed into its surface, bottom and lateral melt components. While our modelling approach is limited in that the sea ice model is not coupled to an atmosphere or ocean model preventing a complete representation of feedback processes, it has the advantage that it disentangles model physics uncertainty from the internal variability inherent to a fully coupled model. The reference simulation of this stand-alone sea ice-mixed layer model was still able to simulate accurately the mean state, trends and inter-annual variability of the main Arctic sea ice cover characteristics (ice area, extent and volume).

Our sensitivity study demonstrates that the various sea ice parameterization schemes

have the potential to significantly impact the sea ice and mixed layer characteristics on regional and basin scales. Introducing a prognostic mixed layer (ML) resulted in an overall decrease of sea ice across the Arctic (in both thickness and concentration). In this simulation, ice growth is reduced due to entrainment of warm water from the deeper ocean as the ML deepens from December to May, while ice growth is enhanced in Autumn due to a more rapid cooling of the shallow ML. Switching off the form drag parameterization increased ice thickness ($\sim +1$ m) over the heavily ridged regions north of Greenland and the Canadian Archipelago and reduced ice thickness (~ -0.25 m) over the Russian continental shelves. We attribute this to the decreased (increased) surface and bottom melt in the former (latter) regions, due to the increased momentum and heat transfer coefficients in these deformed (undeformed) areas. The impact of the 3 equation boundary conditions was localized in the marginal ice zone and acts exclusively during summer, when the temperature difference between the ML and the ice-ocean interface that drives the bottom melt is reduced. The halodynamic brine drainage scheme resulted in a strong reduction in ice thickness (≥ 1 m), due to reduced flushing of melt ponds which lowers the surface albedo and thus results in additional absorption of solar radiation, increasing surface and bottom melt. Conversely, switching off the explicit melt pond scheme resulted in a large increase in sea ice thickness and concentration. Introducing the new parameterization of lateral melt resulted in a large increase in lateral melt over the ice edge that is accompanied by a reduction in bottom melt. Across all simulations, we find that bottom melt accounts typically for around two thirds of the total melt, surface melt accounts for nearly one third and lateral melt accounts for less than 10%.

Quantitative optimization of the simulated sea ice and mixed layer against observations was not the primary goal of this study, and is a topic that will be pursued in future work in stand alone and ice-ocean coupled simulations. Nevertheless, this study reveals that such optimization is complex, and will likely require a trade-off between accurately simulating the mean ice state characteristics and capturing the inter-annual ice state variability. The sen-

sitivity of the inter-annual variability to different sea ice physics parameterization schemes, alludes to the importance of accurate sea ice physics representation in climate models, especially when seeking skillfull seasonal sea ice forecasts. In particular, the difficulty in current sea ice models to reproduce and forecast years with anomalously high or low sea ice extent (Stroeve et al. 2014) is likely due to deficiencies in the physical representation of sea ice in these models. Moreover, the wide spread in the simulated mean state and trend of the main sea ice characteristics in our sensitivity study indicates that model physics uncertainty could dominate overall sea ice uncertainty in general circulation models (Massonnet et al. 2012).

APPENDIX

5. Appendix : Impact of floe size distribution on lateral melt

(iv) Some preliminary equations and definitions

Defining $n_r(r)dr$ as the area fraction covered by ice of size r one has the number of floes of size r per unit area as $\frac{n_r(r)}{\pi r^2}$. To express $n_r(r)$ as a function of the floe area distribution $n_s(s)$ with $s = \pi r^2$ we need the identity:

$$n_s(s) = \frac{n_r(\sqrt{s/\pi})}{2\pi\sqrt{s/\pi}} \tag{5.1}$$

From now on we use the simplified notation $n(r)$ instead of $n_r(r)$. We have the condition of normalization for $n(r)$:

$$\int_0^\infty n(r)dr = 1 \tag{5.2}$$

For a total surface of ice A we can express the first average floe size $\overline{r}_1$ as:

$$\overline{r} = \int_0^\infty A\frac{n(r)}{\pi r^2} r dr / \int_0^\infty S\frac{n(r)}{\pi r^2} dr. \tag{5.3}$$

Note that $\int_0^\infty A\frac{n(r)}{\pi r^2} dr$ is the total number of floes in that area S. Lets choose 2 function $n(r)$ one for a fixed floe size case ($n_1(r)$) and one for a power law FSD ($n_2(r)$). We also assume that both have the same average floe size $\overline{r}$. For the fixed floe size case, the normalization equation (5.2) is satisfied for $n_1(r) = \delta(r - \overline{r})$. The normalization equation for $n_2(r)$ gives:

$$\int_0^\infty n_2(r) dr = \int_0^\infty C r^{-\zeta} dr = \int_{r_{min}}^\infty C r^{-\zeta} dr = C\frac{r_{min}^{-\zeta+1}}{\zeta - 1} = 1. \tag{5.4}$$

Therefore one can write:

$$n_2(r) = (\zeta - 1) r^{-\zeta} r_{min}^{\zeta-1}. \tag{5.5}$$

Now the condition (5.3) can be written:

$$\int_0^\infty A\frac{n_2(r)}{\pi r^2} r dr / \int_0^\infty A\frac{n_2(r)}{\pi r^2} dr = \int_0^\infty r^{-\zeta-1} / \int_0^\infty r^{-\zeta-2} = \frac{\zeta + 1}{\zeta} r_{min} = \overline{r}. \tag{5.6}$$

And we can write r_{min} as a function of $\overline{r}$.

(v) On why power law FSD melt less ice laterally than fixed floe size.

We know that the rate of lateral melting of the total ice area is proportional to the total perimeter P of the floes:

$$\frac{\partial A}{\partial t} = -mP = -m\frac{P}{A}A, \tag{5.7}$$

where m is the lateral rate of melt (in cm/s). Lets calculate this perimeter for the two situations described above. Note both have the same average floe size $\overline{r}$. We have

$$P_1 = 2A\frac{1}{\overline{r}}, \tag{5.8}$$

and

$$P_2 = A \int_0^\infty \frac{n_2(r)}{\pi r^2} 2\pi r dr = 2A \frac{(\zeta - 1)(\zeta + 1)}{\zeta^2} \frac{1}{\overline{r}} = 2P_0(\zeta) A \frac{1}{\overline{r}}. \tag{5.9}$$

Typical observed values of ζ are in the range 0 to 2. But the total area of ice diverges if $\zeta < 1$ and one needs to introduce a upper floe size cutoff value. Example values in this range for the function P_0 are $P_0(2.0) = 0.75$, $P_0(1.75) = 0.67$, $P_0(1.5) = 0.56$, $P_0(1.25) = 0.36$, $P_0(1.1) = 0.17$ amd $P_0(1.0) = 0$. Herman 2010 introduces a different function P_0 that takes the values $P_0(2.0) = 1$, $P_0(1.75) = 0.86$, $P_0(1.5) = 0.67$, $P_0(1.25) = 0.4$, $P_0(1.1) = 0.18$ and $P_0(1.0+) = 0$

We would like to acknowledge the Natural Environment Research Council for supporting this work.

NCEP Reanalysis 2 data were provided by the NOAA NationalWeather Service, USA, from their website at `http://nomads.ncep.noaa.gov/txt_descriptions/servers.shtml`.

REFERENCES

Bitz, C. and W. Lipscomb, 1999: An energy-conserving thermodynamic model of sea ice. *Journal of Geophysical Research*, **104 (15)**, 669–15.

Bitz, C. M., P. R. Gent, R. A. Woodgate, M. M. Holland, and R. Lindsay, 2006: The influence of sea ice on ocean heat uptake in response to increasing CO2. *J. Climate*, **19 (11)**, 2437–2450.

Briegleb, B. and B. Light, 2007: A delta-eddington multiple scattering parameterization for solar radiation in the sea ice component of the community climate system model. ncar

718 tech. Tech. rep., Note NCAR/TN-472+ STR, National Center for Atmospheric Research,
719 2007.

720 Comiso, J. C., 2000, updated 2014: Bootstrap sea ice concentrations from Nimbus-7 SMMR
721 and DMSP SSM/I-SSMIS Version 2 [1980-2013], Boulder, Colorado USA: NASA DAAC
722 at the National Snow and Ice Data Center..

723 Comiso, J. C., 2011: Large Decadal Decline of the Arctic Multiyear Ice Cover. *J. Climate*,
724 **25**, 1176–1193.

725 Coon, M., R. Kwok, G. Levy, M. Pruis, H. Schreyer, and D. Sulsky, 2007: Arctic ice dy-
726 namics joint experiment (aidjex) assumptions revisited and found inadequate. *Journal of*
727 *Geophysical Research-Oceans*, **112 (C11)**, C11S90.

728 Ebert, E. E. and J. A. Curry, 1993: An intermediate one-dimensional thermodynamic sea ice
729 model for investigating ice-atmosphere interactions. *J. Geophys. Res.*, **98 (C6)**, 10 085–
730 10 109.

731 Feltham, D. , 2008: Sea ice rheology. *Annual Review of Fluid Mechanics*

732 Feltham, D. L., N. Untersteiner, J. S. Wettlaufer, and M. G. Worster, 2006: Sea ice is a
733 mushy layer. *Geophys. Res. Lett.*, **40**, 91–112.

734 Ferry, N., S. Masina, A. Storto, K. Haines, M. Valdivieso, B. Barnier, and J.-M. Molines,
735 2011: Product user manual global-reanalysis-phys-001-004-a and b, myocean. Tech. rep.

736 Flocco, D., D. Schroeder, D. L. Feltham, and E. C. Hunke, 2012: Impact of melt ponds on
737 arctic sea ice simulations from 1990 to 2007. *J. Geophys. Res.*, **117 (C9)**, C09 032–.

738 Herman, A., 2010: Sea-ice floe-size distribution in the context of spontaneous scaling emer-
739 gence in stochastic systems. *Phys. Rev. E*, **81 (6)**, 066 123–.

740 Hibler, W., J. Hutchings, and C. Ip, 2006: Sea-ice arching and multiple flow states of arctic
741 pack ice. *Annals of Glaciology*, **44 (1)**, 339–344.

Hunke, E. and J. Dukowicz, 2002: The elastic-viscous-plastic sea ice dynamics model in general orthogonal curvilinear coordinates on a sphere - incorporation of metric terms. *Monthly weather review*.

Hunke, E. C., 2014: Weighing the importance of surface forcing on sea ice - a september 2007 modeling study. *Q.J.R. Meteorol. Soc.*, n/a–n/a.

Hunke, E. C., D. A. Hebert, and O. Lecomte, 2013: Level-ice melt ponds in the los alamos sea ice model, cice. *Ocean Modelling*, **71 (0)**, 26–42.

Hunke, E. C., W. H. Lipscomb, A. K. Turner, N. Jeffery, and S. Elliott, 2013: CICE: the Los Alamos Sea Ice Model Documentation and Software User's Manual Version 5.0.

Johnson, M., S. Gaffigan, E. Hunke, and R. Gerdes, 2007: A comparison of arctic ocean sea ice concentration among the coordinated aomip model experiments. *Journal of Geophysical Research: Oceans (1978–2012)*, **112 (C4)**.

Kanamitsu, M. , Ebisuzaki, W. , Woollen, J. , Yang, S. , Hnilo, J. J., Fiorino, M. and Potter, G. L., 2002: NCEP-DOE AMIP-II Reanalysis (R-2). *Bull. Amer. Meteor. Soc.*, **83** 1631–1643.

Keen, A. B., H. T. Hewitt, J. K. Ridley, 2013: A case study of a modelled episode of low Arctic sea ice. *Clim. Dyn.*, **41** 1229–1244.

Kwok, R. and D. A. Rothrock, 2009: Decline in Arctic sea ice thickness from submarine and ICESat records: 1958–2008. *Geophys. Res. Lett.*, 2009GL036 L15501–.

Kraus, E. B. and J. S. Turner, 1967: A one-dimensional model of the seasonal thermocline ii. the general theory and its consequences. *Tellus*, **19 (1)**, 98–106.

Laxon, S. W., L. A. Giles, A. L. Ridout, D. J. Wingham, Duncan J. R. Willatt, R. Cullen, R. Kwok, A. Schweiger, J. Zhang, C. Haas, Christian S. Hendricks, R. Krishfield, N. Kurtz,

765 Nathan, S. Farrell, M. Davidson, 2013: CryoSat-2 estimates of Arctic sea ice thickness
766 and volume. *Geophys. Res. Lett.*, 2013GL036.

767 Lindsay R. and A. Schweiger , 2013: Arctic sea ice thickness loss determined using subsur-
768 face, aircraft, and satellite observations. *The Cryosphere*, **9**, 269–283.

769 Lipscomb, W. and E. Hunke, 2004: Modeling sea ice transport using incremental remapping.
770 *Monthly Weather Review*, **132 (6)**, 1341–1354.

771 Lipscomb, W., E. Hunke, W. Maslowski, and J. Jakacki, 2007: Ridging, strength, and
772 stability in high-resolution sea ice models. *J. Geophys. Res*, **112**.

773 Lu, P., Z. Li, B. Cheng, and M. Leppäranta, 2011: A parameterization of the ice-ocean drag
774 coefficient. *J. Geophys. Res.*, **116 (C7)**, C07 019–.

775 Lüpkes, C., V. M. Gryanik, J. Hartmann, and E. L. Andreas, 2012: A parametrization, based
776 on sea ice morphology, of the neutral atmospheric drag coefficients for weather prediction
777 and climate models. *J. Geophys. Res.*, **117 (D13)**, D13 112–.

778 Maslowski, W., J. Clement Kinney, M. Higgins, and A. Roberts, 2012: The future of arctic
779 sea ice. *Annu. Rev. Earth Planet. Sci.*, **40 (1)**, 625–654.

780 Massonnet, F., T. Fichefet, H. Goosse, C. M. Bitz, G. Philippon-Berthier, M. M. Holland,
781 and P.-Y. Barriat, 2012: Constraining projections of summer arctic sea ice. *The Cryosphere*
782 *Discussions*, **6 (4)**, 2931–2959.

783 Maykut, G. A. and M. G. McPhee, 1995: Solar heating of the arctic mixed layer. *J. Geophys.*
784 *Res.*, **100 (C12)**, 24 691–24 703.

785 Maykut, G. A. and D. K. Perovich, 1987: The role of shortwave radiation in the summer
786 decay of a sea ice cover. *J. Geophys. Res.*, **92 (C7)**.

McPhee, M. G., 2008: Physics of early summer ice/ocean exchanges in the western weddell sea during ispol. *Deep Sea Research Part II: Topical Studies in Oceanography*, **55**, 1075–1097.

McPhee, M. G., 2012: Advances in understanding ice–ocean stress during and since aidjex. *Cold Regions Science and Technology*, **76**, 24–36.

Notz, D., 2005: Thermodynamic and fluid-dynamical processes in sea ice. Ph.D. thesis, University of Cambridge.

Notz, D., 2012: Challenges in simulating sea ice in earth system models. *WIREs Clim Change*, **3 (6)**, 509–526.

Notz D. , 2013: Sea-ice extent provides a limited metric of model performance. *The Cryosphere*, **7**, 3095–3131.

Overland, J. E. and M. Wang, 2013: When will the summer arctic be nearly sea ice free? *Geophys. Res. Lett.*, **40 (10)**, 20972101.

Peralta-Ferriz, C. and R.A.. Woodgate, 2014: Seasonal and interannual variability of pan-Arctic surface mixed layer properties from 1979 to 2012 from hydrographic data, and the dominance of stratification for multiyear mixed layer depth shoaling. *Progress in Oceanography*.

Perovich, D., J. Richter-Menge, C. Polashenski, B. Elder, T. Arbetter, and O. Brennick, 2014: Sea ice mass balance observations from the north pole environmental observatory. *Geophys. Res. Lett.*, 2014GL059 356–.

Perovich, D. K., 1983: On the summer decay of a sea ice cover. Ph.D. thesis, University of Washington.

Petty, A. A., D. L. Feltham, and P. R. Holland, 2012: Impact of atmospheric forcing on antarctic continental shelf water masses. *J. Phys. Oceanogr.*, **43 (5)**, 920–940.

Petty, A. A., P. R. Holland, and D. L. Feltham, 2014: Sea ice and the ocean mixed layer over the antarctic shelf seas. *The Cryosphere*, **8 (2)**, 761–783.

Rae, J.G. L., H. T. Hewitt, A. B. Keen, J. K. Ridley, J. M. Edwards, C. M. Harris, 2014: A sensitivity study of the sea ice simulation in the global coupled climate model, HadGEM3 . *Ocean Modelling*, **74**, 60–76.

Rampal, P., J. Weiss, D. Marsan, and M. Bourgoin, 2009: Arctic sea ice velocity field: General circulation and turbulent-like fluctuations. *J. Geophys. Res.*, **114**, C10014–.

Rampal, P., J. Weiss, C. Dubois, and J.-M. Campin, 2011: Ipcc climate models do not capture arctic sea ice drift acceleration: Consequences in terms of projected sea ice thinning and decline. *J. Geophys. Res.*, **116**, C00D07–.

Richter-Menge, J.A., D.K. Perovich, C. Dubois, B.C. Elder, K. Claffey, I. Rigor, and M. Ortmeyer, 2011: Ice mass-balance buoys: a tool for measuring and attributing changes in the thickness of the Arctic sea-ice cover. *Annals of Glaciology*, **44 (1)**, 205–210.

Rothrock, D., 1975: The energetics of the plastic deformation of pack ice by ridging. *Journal of Geophysical Research-Oceans*, **80 (33)**.

Schmidt, G. A., C. M. Bitz, U. Mikolajewicz, and L.-B. Tremblay, 2004: Ice-ocean boundary conditions for coupled models. *Ocean Modelling*, **7 (1??2)**, 59–74.

Schröder, D., D. L. Feltham, D. Flocco, and M. Tsamados, 2014: September arctic sea-ice minimum predicted by spring melt-pond fraction. *Nature Clim. Change*, **4 (5)**, 353–357.

Schröder, D., T. Vihma, A. Kerber, and B. Brmmer, 2003: On the parameterization of turbulent surface fluxes over heterogeneous sea ice surfaces. *J. Geophys. Res.*, **108 (C6)**, 3195–.

Spreen, G., R. Kwok, and D. Menemenlis, 2011: Trends in Arctic sea ice drift and role of wind forcing: 1992-2009. *Geophys. Res. Lett.*, 2011GL038 L19501–.

Steele, M., 1992: Sea ice melting and floe geometry in a simple ice-ocean model. *J. Geophys. Res.*, **97 (C11)**, 17 729–17 738.

Steele, M., J. H. Morison, and N. Untersteiner, 1989: The partition of air-ice-ocean momentum exchange as a function of ice concentration, roe size, and draft. *J. Geophys. Res.*, **94 (C9)**, 12 739–12 750.

Steele, M., J. Zhang, and W. Ermold, 2010: Mechanisms of summertime upper arctic ocean warming and the effect on sea ice melt. *J. Geophys. Res.*, **115 (C11)**, C11 004–.

Stroeve, J., L. C., V. Kattsov and A. Barrett, M. Serreze, T. Pavlova, M. Holland, W. N.Meier, 2012: Trends in Arctic sea ice extent from CMIP5, CMIP3 and observations. *Geophys. Res. Lett.*, 2012GL039 L16502–.

Stroeve, J., L. C. Hamilton, C. M. Bitz, and E. Blanchard-Wrigglesworth, 2014: Predicting september sea ice ensemble skill of the search sea ice outlook 2008-2013. *Geophys. Res. Lett.*, 2014GL059 388–.

Strong, C. and I. G. Rigor, 2013: Arctic marginal ice zone trending wider in summer and narrower in winter. *Geophys. Res. Lett.*, 2013GL040 4864–4868.

Toole, J. M., M.-L. Timmermans, D. K. Perovich, R. A. Krishfield, A. Proshutinsky, and J. Richter-Menge, 2010: Influences of the ocean surface mixed layer and thermohaline stratification on arctic sea ice in the central canada basin. *Journal of Geophysical Research: Oceans (1978–2012)*, **115 (C10)**

Toole, J. M., R. A. Krishfield, M.-L. Timmermans, and A. Proshutinsky, 2011: The Ice-Tethered Profiler: Argo of the Arctic. *Oceanography (1978–2012)*, **24 (3)**, 126–135.

Tsamados, M., D. L. Feltham, D. Schroeder, D. Flocco, S. L. Farrell, N. Kurtz, S. W. Laxon, and S. Bacon, 2014: Impact of variable atmospheric and oceanic form drag on simulations of arctic sea ice*. *J. Phys. Oceanogr.*, **44 (5)**, 1329–1353.

Tsamados, M., D. L. Feltham, and A. V. Wilchinsky, 2013: Impact of a new anisotropic rheology on simulations of arctic sea ice. *Journal of Geophysical Research: Oceans*, **118 (1)**, 91–107.

Turner, A. K. and E. Hunke, 2015: Impacts of a mushy-layer thermodynamic approach in global sea-ice simulations using the cice sea-ice model. *Journal of Geophysical Research: Oceans*, **120 (2)**, 1253–1275.

Turner, A. K., E. C. Hunke, and C. M. Bitz, 2013: Two modes of sea-ice gravity drainage: A parameterization for large-scale modeling. *J. Geophys. Res. Oceans*, **118 (5)**, 2279–2294.

Weiss, J. and D. Marsan, 2004: Scale properties of sea ice deformation and fracturing. *Comptes rendus-Physique*, **5 (7)**, 735–751.

Williams, T. D., L. G. Bennets, V. A. Squire, D. Dumont, and L. Bertino, 2013: Wave-ice interactions in the marginal ice zone. Part 1: Theoretical foundations. *Ocean Modelling*, **71 (0)**, 81–91.

6. Figures & Tables

Name	Description
REF	Reference run: prognostic ML (Petty et al. 2014)[a], low heat transfer coefficient $\alpha_h = C_{dw}/2$, form drag (Tsamados et al. 2014), fixed floe size ($L = 300$m), thermodynamics and flushing of Turner and Hunke (2015)[a], 3 equation boundary condition[c]
MLD_CST	As *REF* but default prescribed ML ($h_{mix} = 20$m) [b]
MLD_MIN_2M	As *REF* but $h_{mix}^{min} = 2$m instead of default $h_{mix}^{min} = 10$m[a]
NO_3EQTN	As *REF* but default boundary condition $T_0 = T_f(S_{mix})$[c]
NO_MUSHY	As *REF* but thermodynamics of Bitz and Lipscomb (1999) and default boundary condition $T_0 = T_f(S_{mix})$[c]
DBL_ALPHA_H	As *REF* but $\alpha_h = C_{dw}$[c]
DBL_ALPHA_H / NO_3EQTN	As *REF* but doubling heat transfer coefficient $\alpha_h = C_{dw}$ and default boundary condition $T_0 = T_f(S_{mix})$[c]
DBL_ALPHA_H / NO_MUSHY	As *REF* but doubling heat transfer coefficient $\alpha_h = C_{dw}$, thermodynamics of Bitz and Lipscomb (1999), and default boundary condition $T_0 = T_f(S_{mix})$[c]
NO_POND	As *REF* but melt ponds area and thickness set to zero[d]
FALSE_BOTTOM	As *REF* but Thermodynamics of Bitz and Lipscomb (1999), $T_0 = T_f(S_{mix})$[c], $\alpha_h = C_{dw}$ but $\alpha_h = C_{dw}/2$ if $A_p \geq 20\%$ in ad-hoc description of false bottoms [d]
NO_FORM_DRAG	As *REF* but $C_{da} = 1.2 \times 10^{-3}$, $C_{dw} = 6.09 \times 10^{-3}$ SKIN setup of Tsamados et al. (2014) [e]
LAT_MELT	As *REF* but Power law FSD with average floe size $L(A)$, [f]
SST_TIME	As *REF* but Temperature restoring towards a time dependent MYO SST[a]
SFFT14	Setup of Schröder et al. (2014) (fixed ML depth, $\alpha_h = 0.006$).

[a] See section 2i. All other model runs contain a single modification with respect to REF.

[b] See section 2a.

[c] See section 2iii, note that BF stands here for bottom flux.

[d] See section 2a, note that FB stands here for false bottom.

List of Figures

6 Maps of the climatology of the average July bottom melt over the period 1994 to 2013 for all sensitivity runs. Note that the map for the *REF* model run is given in absolute melt rate values (in cm/day, top color bar) while all other model runs are given as difference in melt rate with respect to *REF* (in cm/day, bottom color bar). 46

7 Maps of the climatology of the average July lateral melt over the period 1994 to 2013 for all sensitivity runs. Note that the map for the *REF* model run is given in absolute melt rate values (in cm/day, top color bar) while all other model runs are given as difference in melt rate with respect to *REF* (in cm/day, bottom color bar). 47

8 August sea ice concentration climatology maps over the period 1994 to 2013 for all sensitivity runs. Note that the map for the *REF* model run is given in absolute concentration values (in %, top color bar) while all other model runs are given as difference in concentration with respect to *REF* (in %, bottom color bar). 48

9 August sea ice thickness climatology maps over the period 1994 to 2013 for all sensitivity runs. Note that the map for the *REF* model run is given in absolute thickness values (metres, in top color bar) while all other model runs are given as difference in thickness with respect to *REF* (metres, in bottom color bar). 49

10 August mixed layer temperature climatology maps over the period 1994 to 2013 for all sensitivity runs. Note that the map for the *REF* model run is given in absolute temperature values (°C, in top color bar) while all other model runs are given in as difference in temperature with respect to *REF* (°C, bottom color bar). 50

11 August mixed layer salinity climatology maps over the period 1994 to 2013 for all sensitivity runs. Note that the map for the *REF* model run is given in absolute salinity values (PSU, top color bar) while all other model runs are given as difference in salinity with respect to *REF* (PSU, bottom color bar). 51

12 Impact of the sensitivity model runs on the total area (a)-(c), total extent (d)-(f) and total volume (g)-(i) of sea ice. Figures on the first column show the seasonal climatology calculated over the period 1993 to 2012 while columns two and three show the time series for August and September. The colour code is a follows: *REF* in red, *MLD_CST* in blue, *SST_TIME* in green, *MLD_MIN_2M* in mauve, *SSMI_NT* and *PIOMAS* in solid black and *SSMI_BT* in dashed black. 52

13 Scatter plots of the trends vs averages over the period 1993 to 2010 of the August total sea ice area (a), sea ice extent (b) and sea ice volume (c). Scatter plots of the full and de-trended correlation coefficients between the model and observed time series of the total sea ice area (d), sea ice extent (d) and sea ice volume (f). Here we correlate model sea ice area and extent with the *SSMI_BT* observation and model volume with *PIOMAS*. We show 13 model runs described in section 2. As a reference we also show values from the model run discussed in Schröder et al. (2014). 53

14 Scatter plots of the trends vs averages over the period 1993 to 2010 of the September total sea ice area (a), sea ice extent (b) and sea ice volume (c). Scatter plots of the full and de-trended correlation coefficients between the model and observed time series of the total sea ice area (d), sea ice extent (e) and sea ice volume (f). Here we correlate model sea ice area and extent with the *SSMI_BT* observation and model volume with *PIOMAS*. We show 13 model runs described in section 2. As a reference we also show values from the model run discussed in Schröder et al. (2014). 54

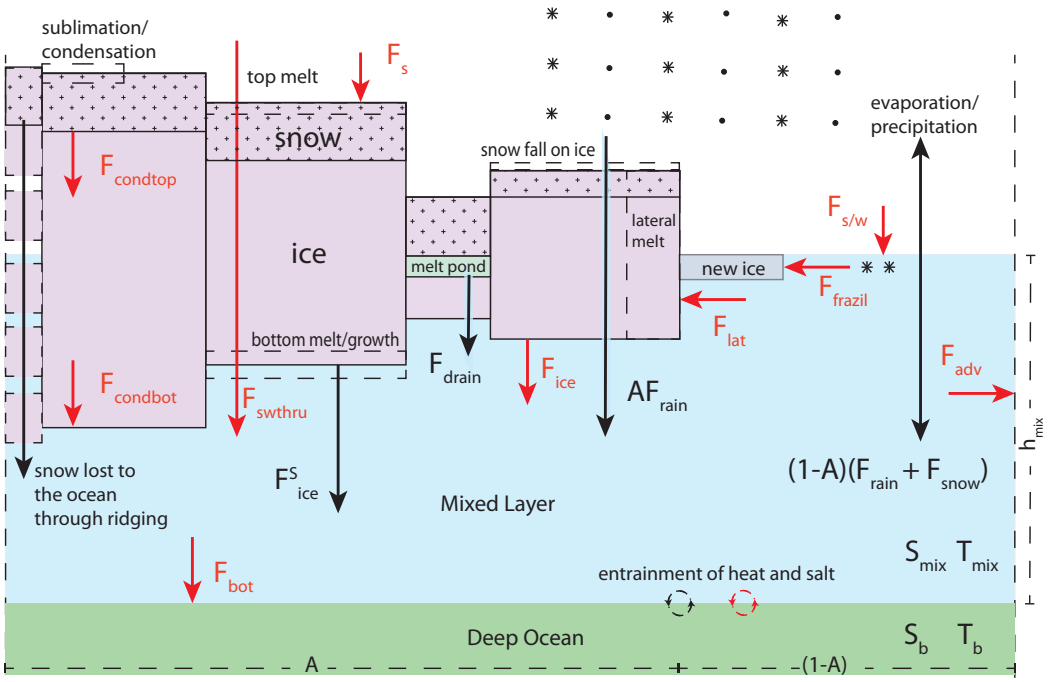

FIG. 1. Schematic of the new prognostic ML module and of the other main thermodynamic processes included in CICE. The main heat fluxes are highlighted in red while the main salt and freshwater fluxes are shown in black. Adapted from Petty et al. (2014).

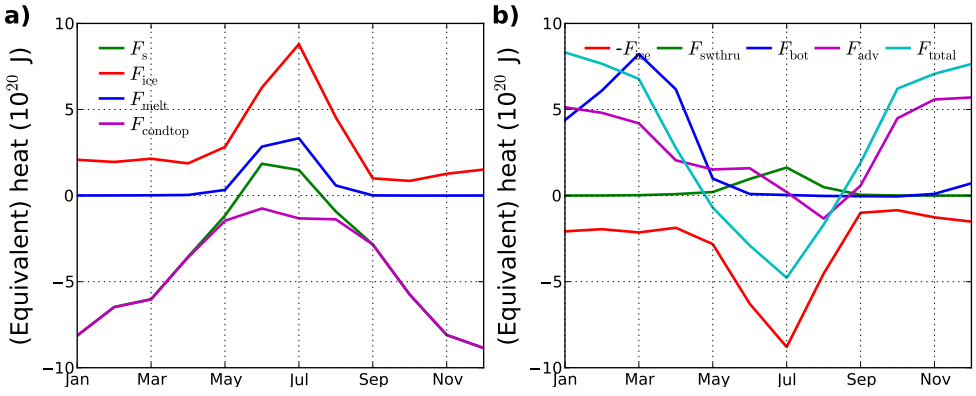

FIG. 2. Climatology of the seasonal cycle of main components of the heat budget of the Arctic sea ice (a) and ML (b) over the period 1993 to 2012. All terms are expressed as an equivalent amount of heat entering the ice or ML (in Joules).

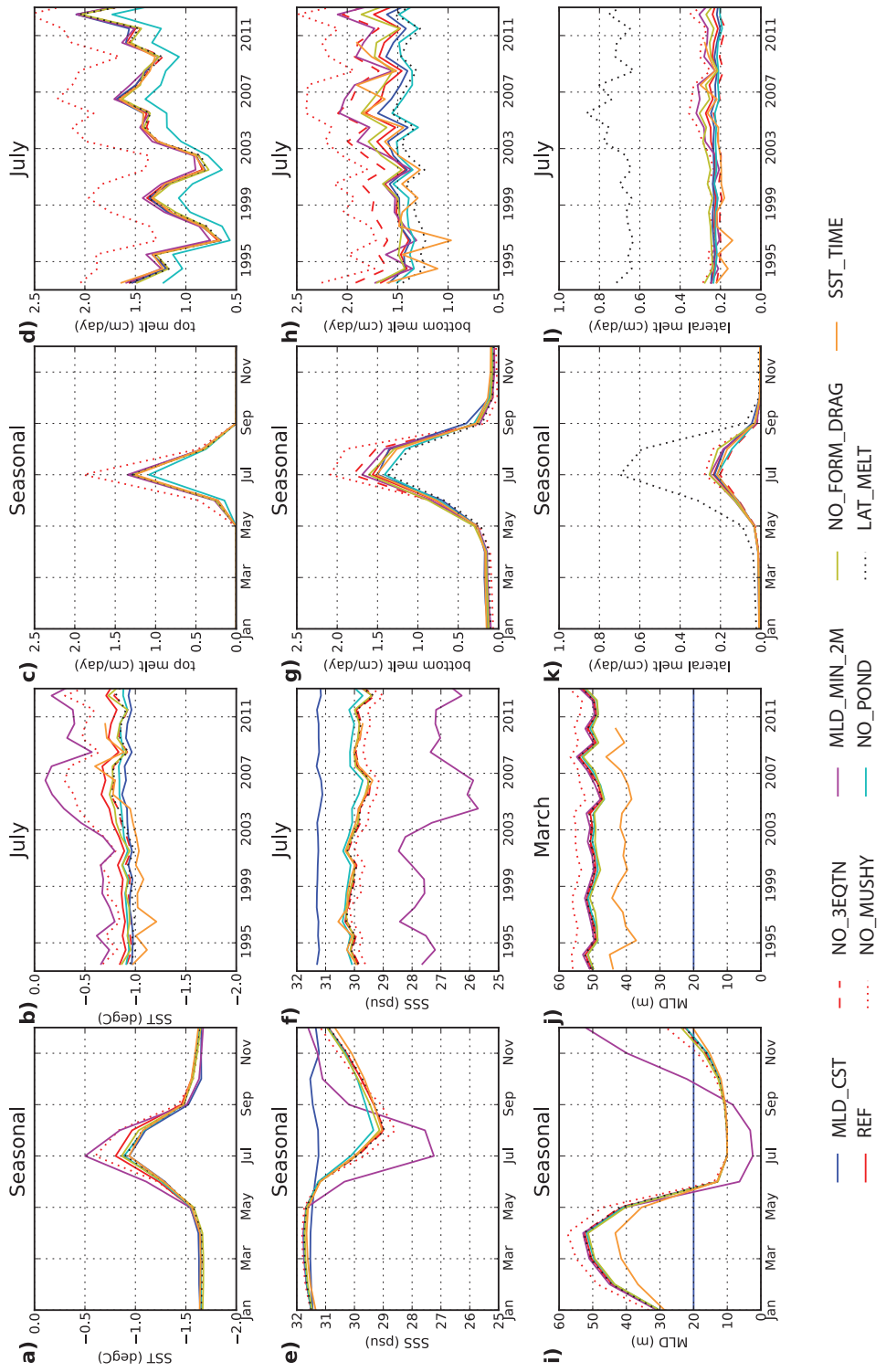

FIG. 3. Impact of the sensitivity model runs on sea surface temperature (a)-(b), sea surface salinity (e)-(f), ML depth (i)-(j), top melt (c)-(d), bottom melt (g)-(h) and lateral melt (k)-(l). Figures on the first and third columns show the seasonal climatology calculated over the period 1993 to 2012 while columns two and four show time series for July (except (j) that shows the MLD in March). The colour code is the same as in figure 2.

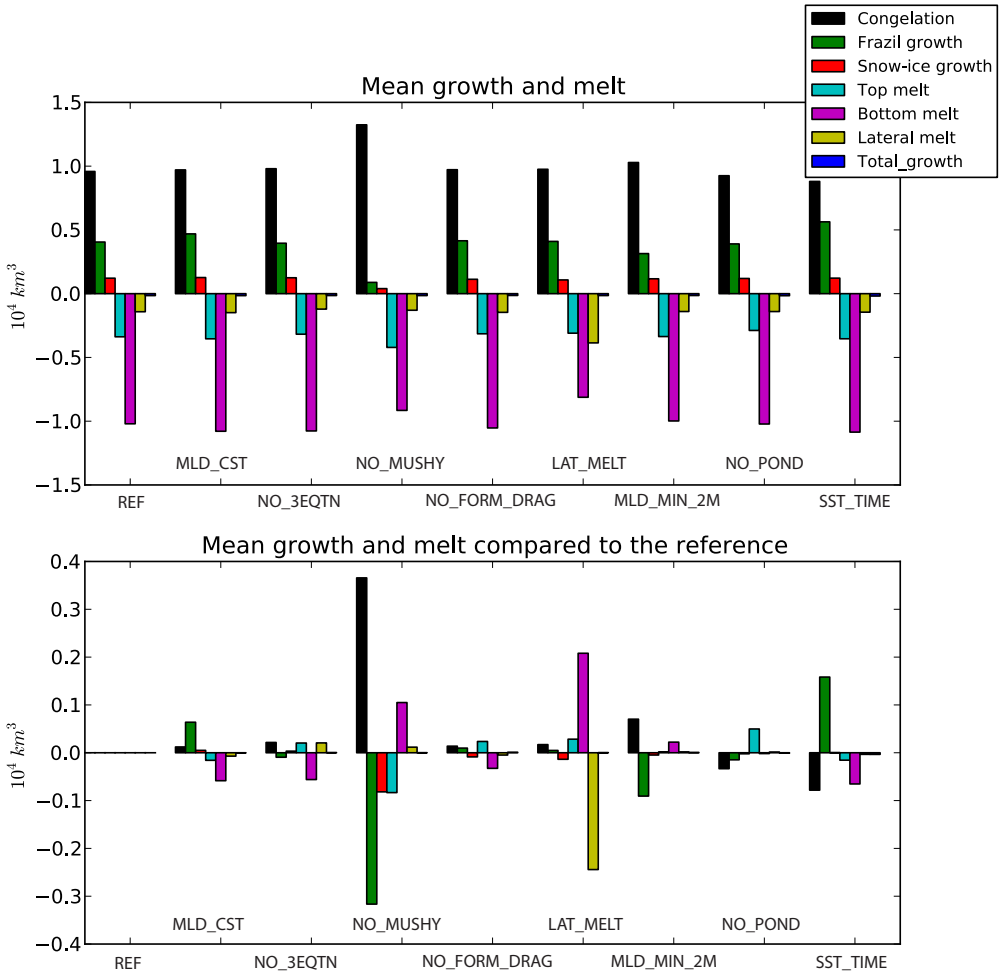

FIG. 4. Mean annual volume of ice gained or lost through thermodynamic processes associated with our collection of models between 1993 and 2010. The incremental differences from the reference run *REF* volume for each process are shown in the second plot; e.g., positive melt terms indicate increased ice volume due to decreased melting, relative to REF. Notice the differing scales in the two plots.

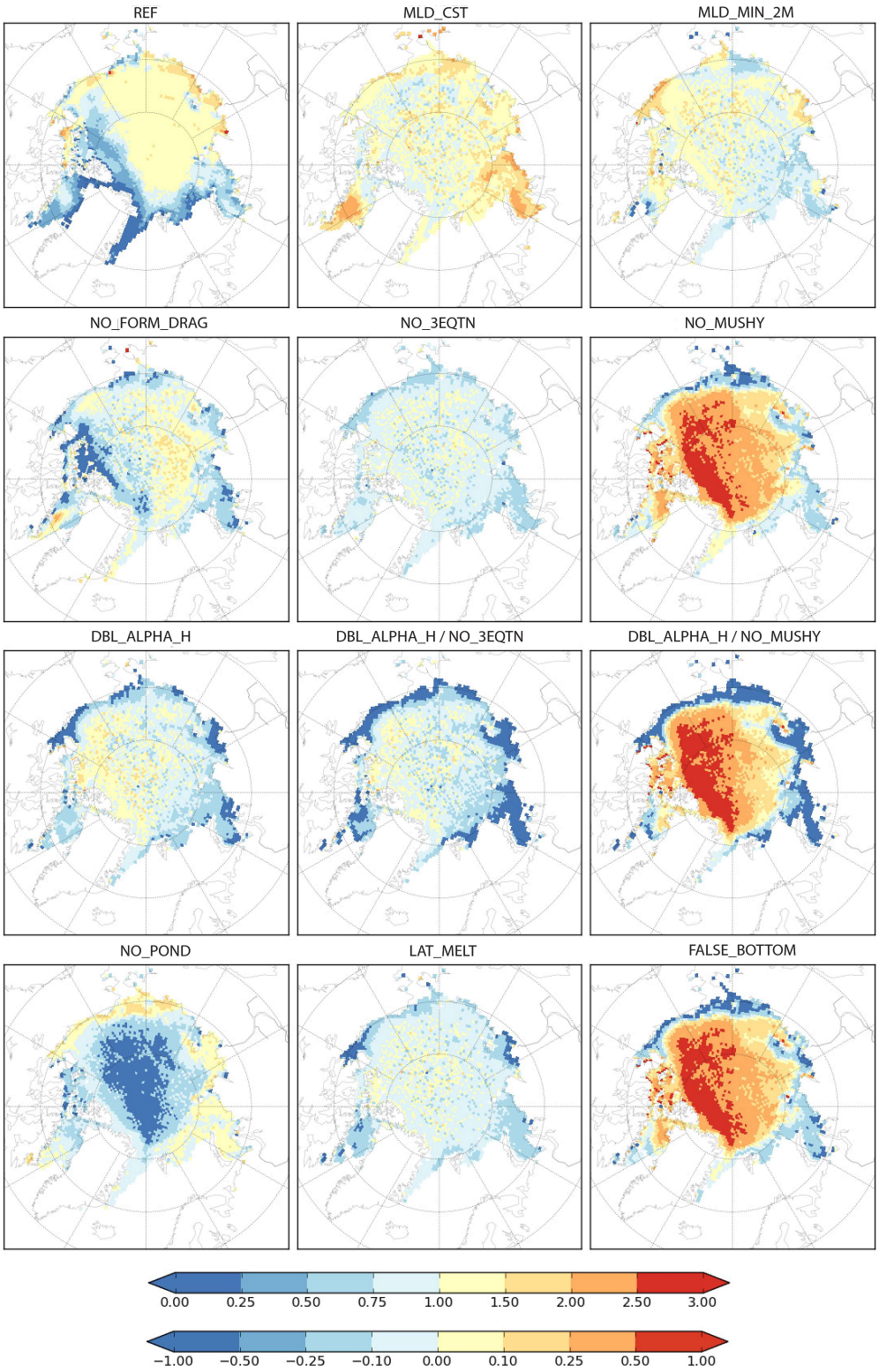

FIG. 5. Maps of the climatology of the average July top melt over the period 1994 to 2013 for all sensitivity runs. Note that the map for the *REF* model run is given in absolute melt rate values (in cm/day, top color bar) while all other model runs are given as difference in melt rate with respect to *REF* (in cm/day, bottom color bar).

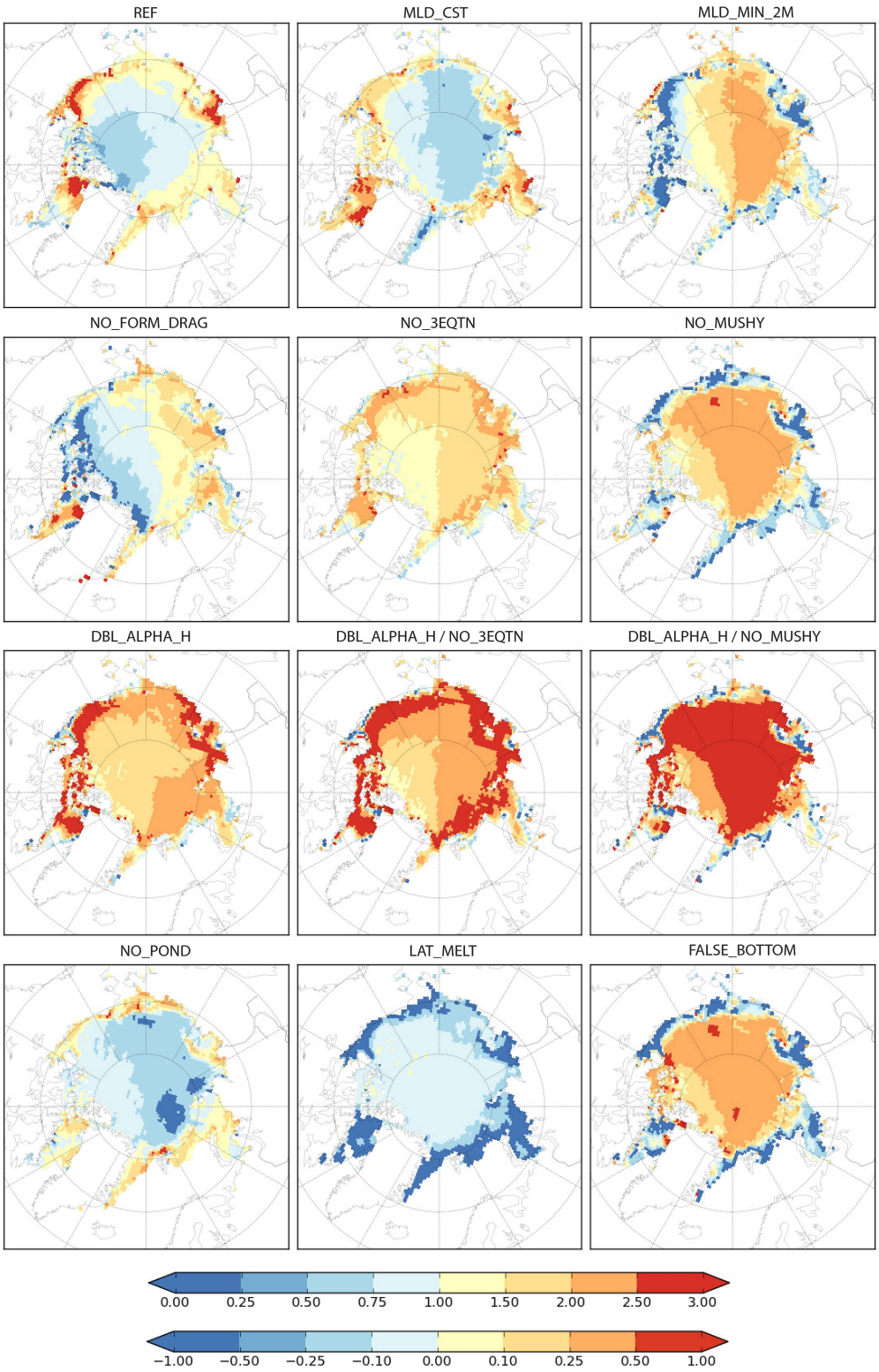

FIG. 6. Maps of the climatology of the average July bottom melt over the period 1994 to 2013 for all sensitivity runs. Note that the map for the *REF* model run is given in absolute melt rate values (in cm/day, top color bar) while all other model runs are given as difference in melt rate with respect to *REF* (in cm/day, bottom color bar).

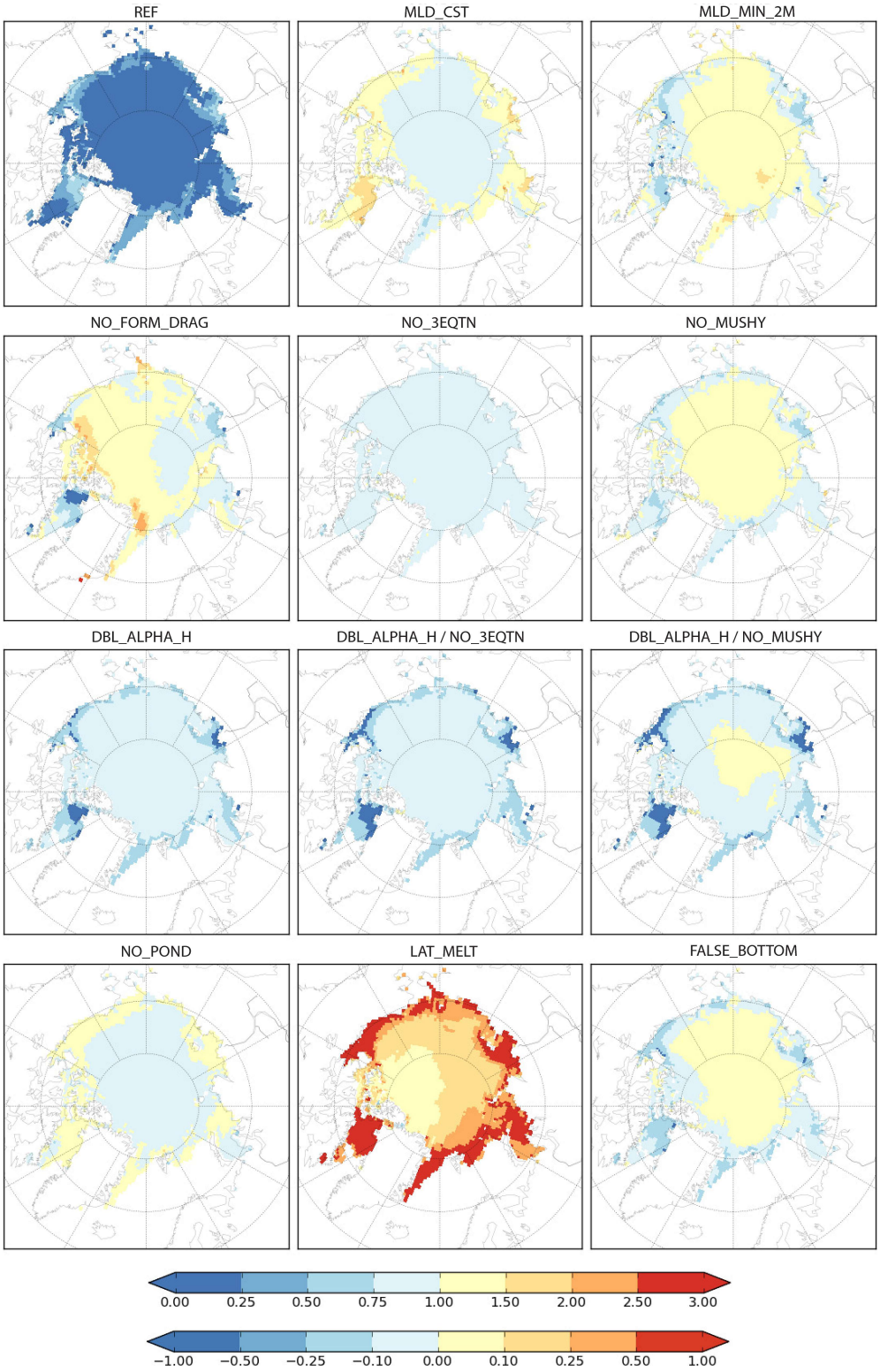

FIG. 7. Maps of the climatology of the average July lateral melt over the period 1994 to 2013 for all sensitivity runs. Note that the map for the *REF* model run is given in absolute melt rate values (in cm/day, top color bar) while all other model runs are given as difference in melt rate with respect to *REF* (in cm/day, bottom color bar).

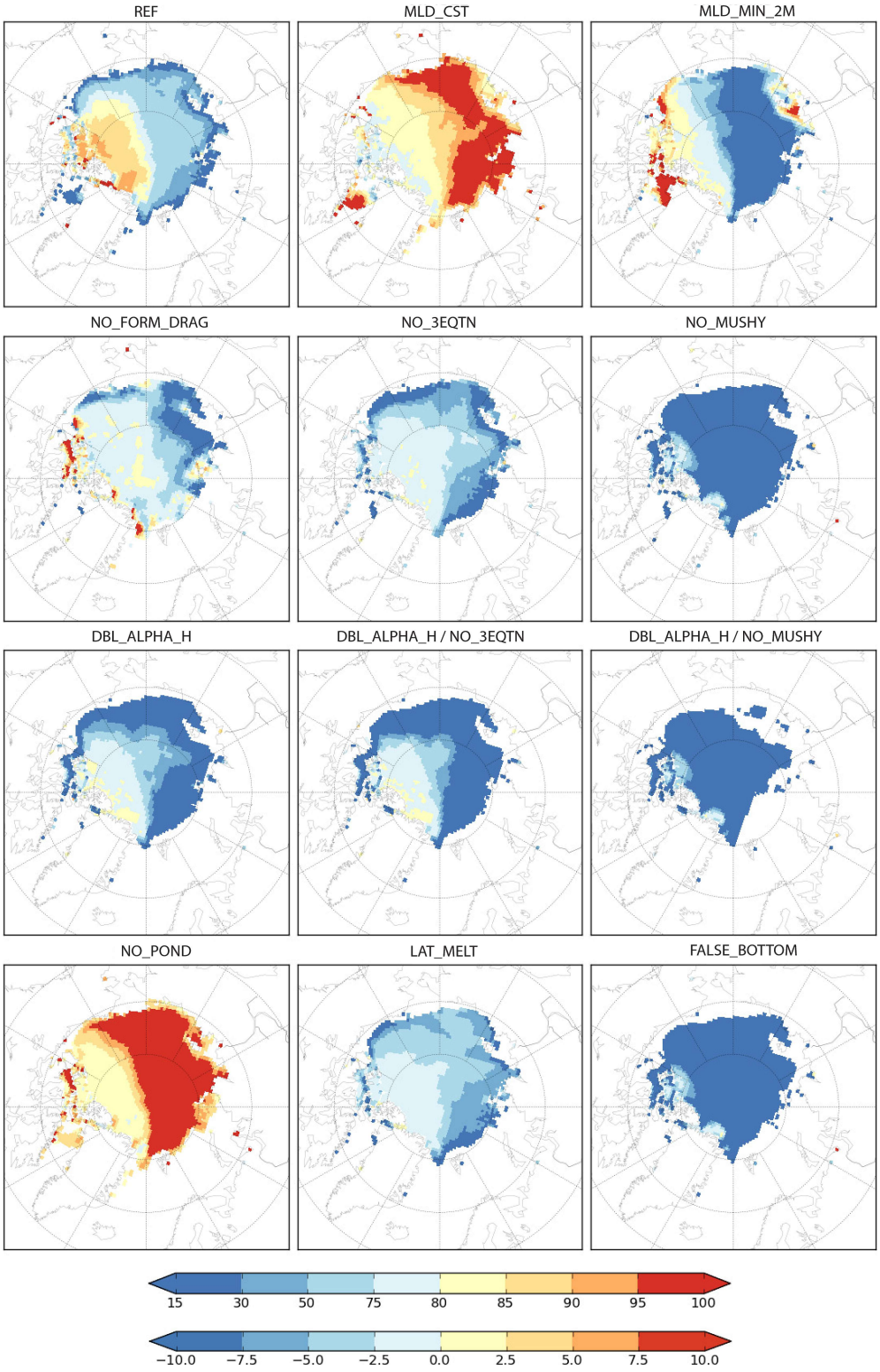

FIG. 8. August sea ice concentration climatology maps over the period 1994 to 2013 for all sensitivity runs. Note that the map for the *REF* model run is given in absolute concentration values (in %, top color bar) while all other model runs are given as difference in concentration with respect to *REF* (in %, bottom color bar).

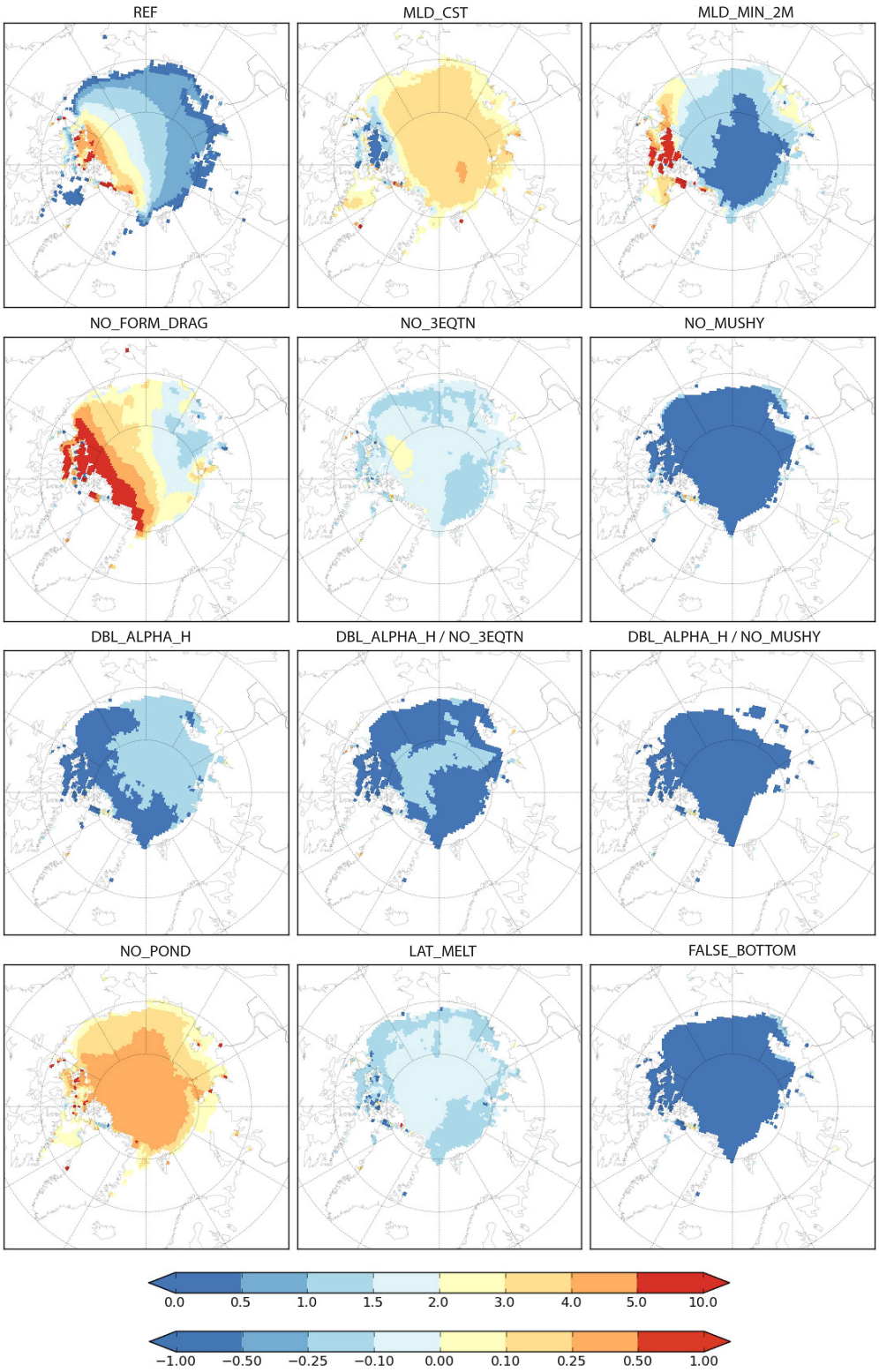

FIG. 9. August sea ice thickness climatology maps over the period 1994 to 2013 for all sensitivity runs. Note that the map for the *REF* model run is given in absolute thickness values (metres, in top color bar) while all other model runs are given as difference in thickness with respect to *REF* (metres, in bottom color bar).

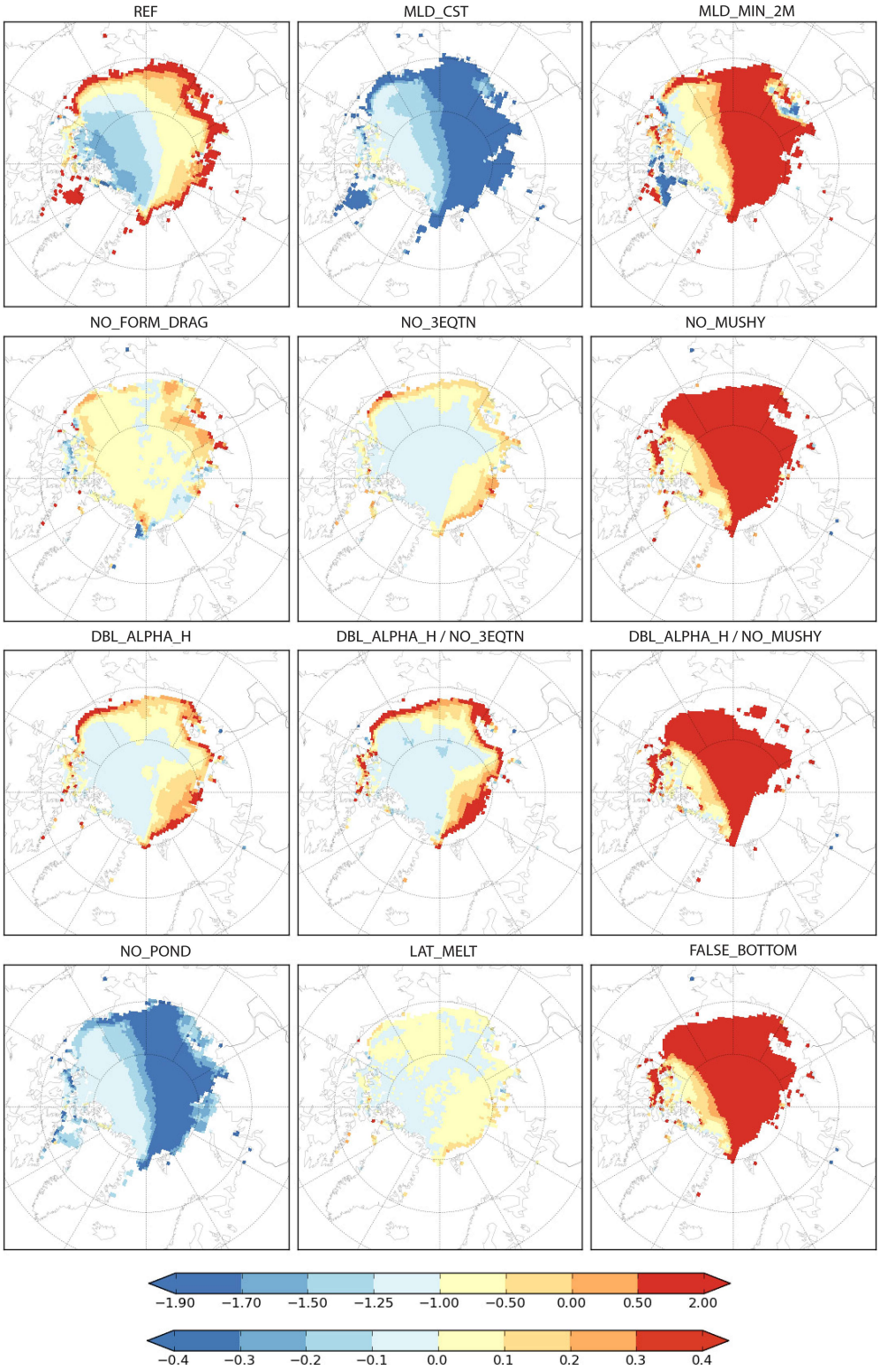

FIG. 10. August mixed layer temperature climatology maps over the period 1994 to 2013 for all sensitivity runs. Note that the map for the *REF* model run is given in absolute temperature values (°C, in top color bar) while all other model runs are given in as difference in temperature with respect to *REF* (°C, bottom color bar).

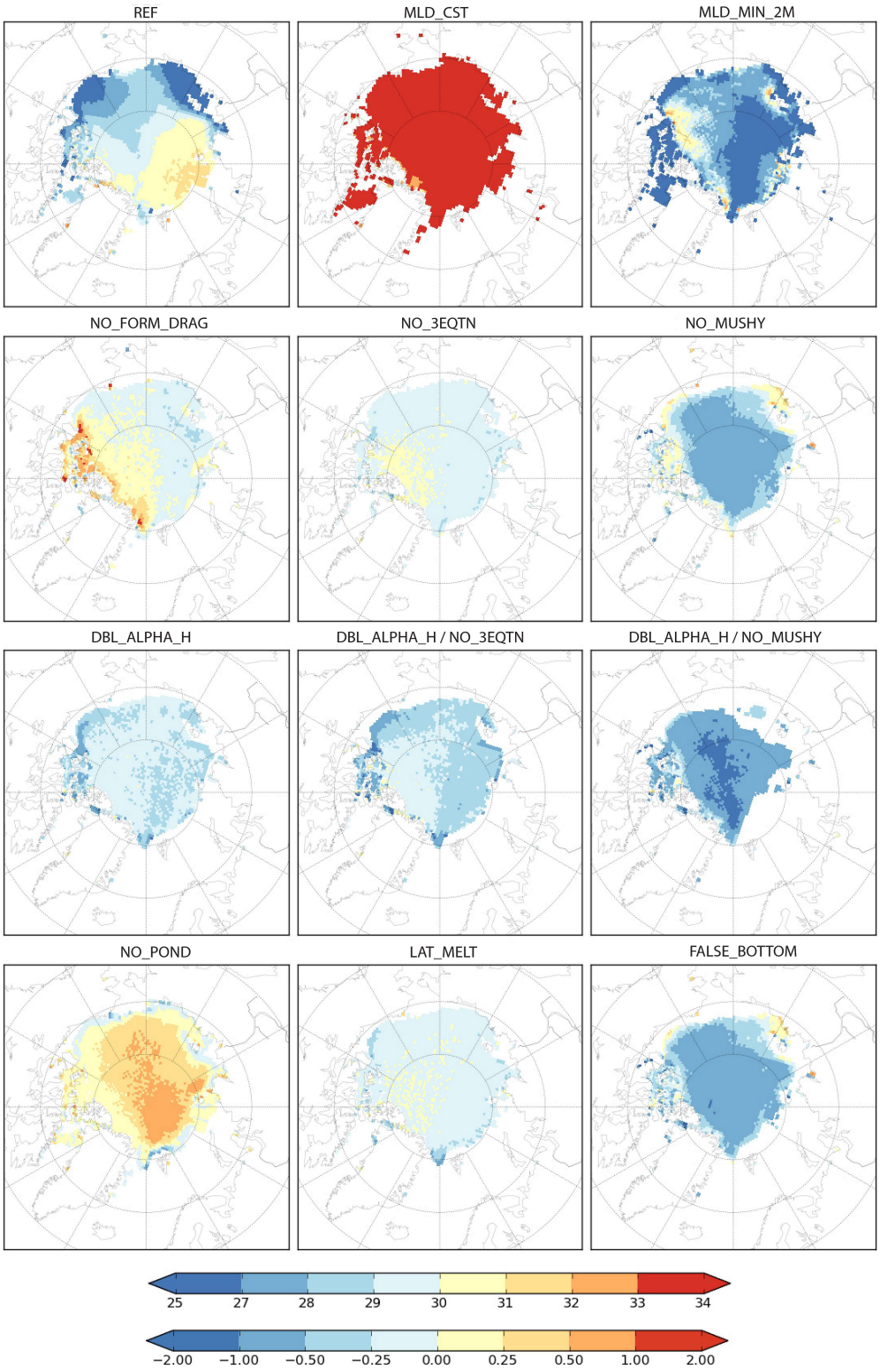

FIG. 11. August mixed layer salinity climatology maps over the period 1994 to 2013 for all sensitivity runs. Note that the map for the *REF* model run is given in absolute salinity values (PSU, top color bar) while all other model runs are given as difference in salinity with respect to *REF* (PSU, bottom color bar).

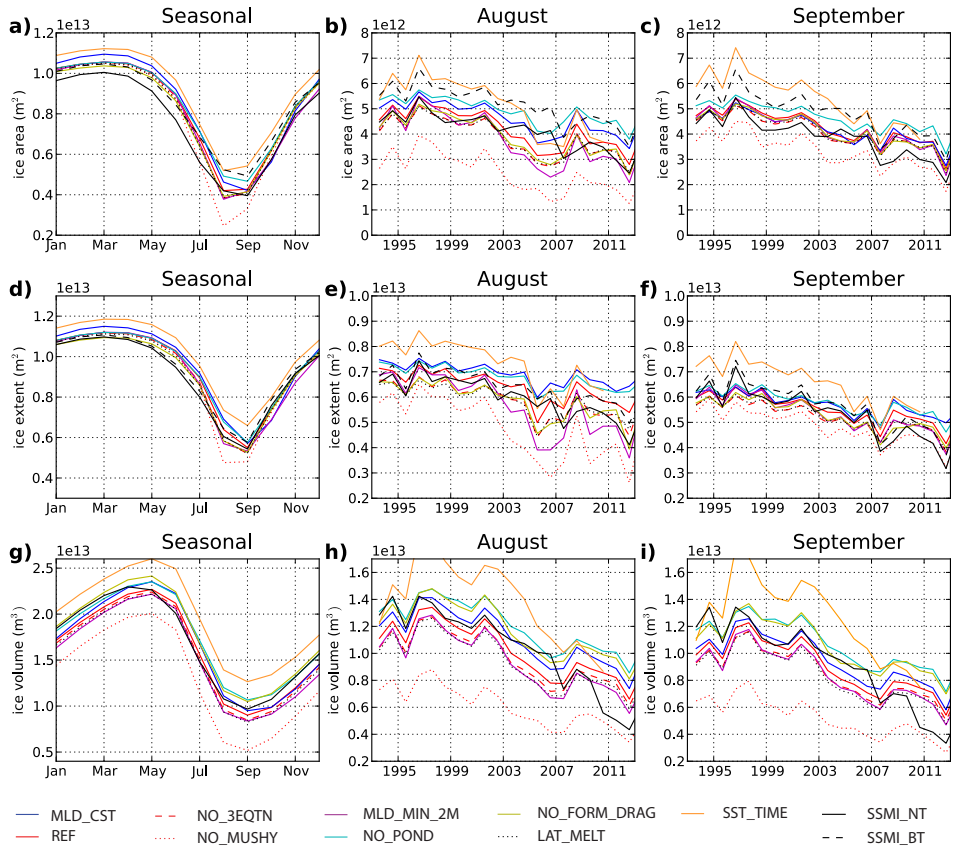

FIG. 12. Impact of the sensitivity model runs on the total area (a)-(c), total extent (d)-(f) and total volume (g)-(i) of sea ice. Figures on the first column show the seasonal climatology calculated over the period 1993 to 2012 while columns two and three show the time series for August and September. The colour code is a follows: *REF* in red, *MLD_CST* in blue, *SST_TIME* in green, *MLD_MIN_2M* in mauve, *SSMI_NT* and *PIOMAS* in solid black and *SSMI_BT* in dashed black.

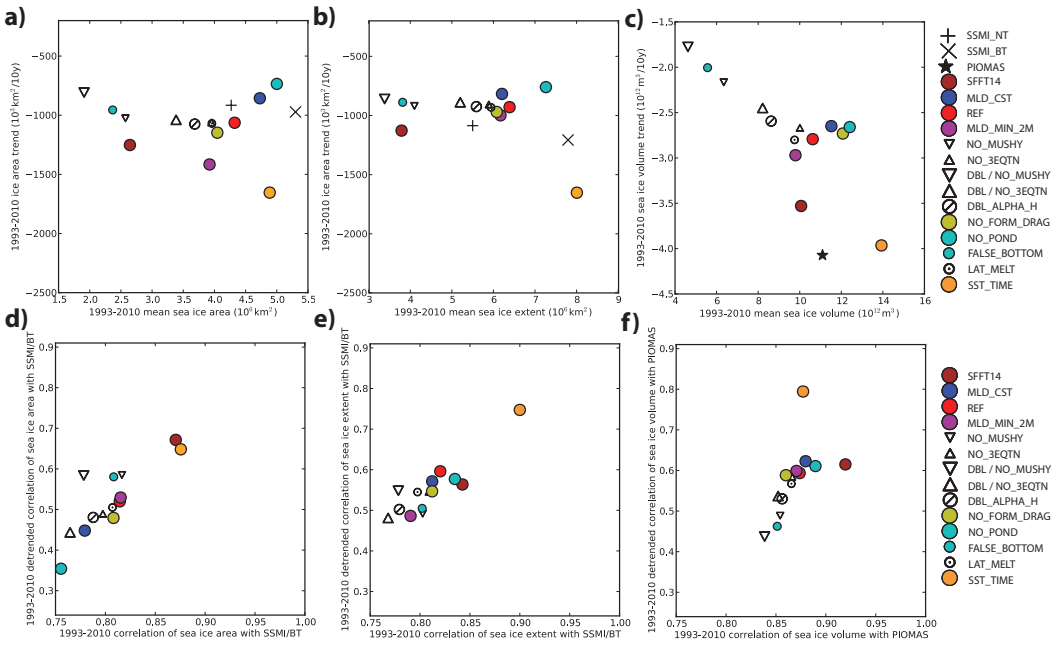

FIG. 13. Scatter plots of the trends vs averages over the period 1993 to 2010 of the August total sea ice area (a), sea ice extent (b) and sea ice volume (c). Scatter plots of the full and de-trended correlation coefficients between the model and observed time series of the total sea ice area (d), sea ice extent (d) and sea ice volume (f). Here we correlate model sea ice area and extent with the *SSMI_BT* observation and model volume with *PIOMAS*. We show 13 model runs described in section 2. As a reference we also show values from the model run discussed in Schröder et al. (2014).

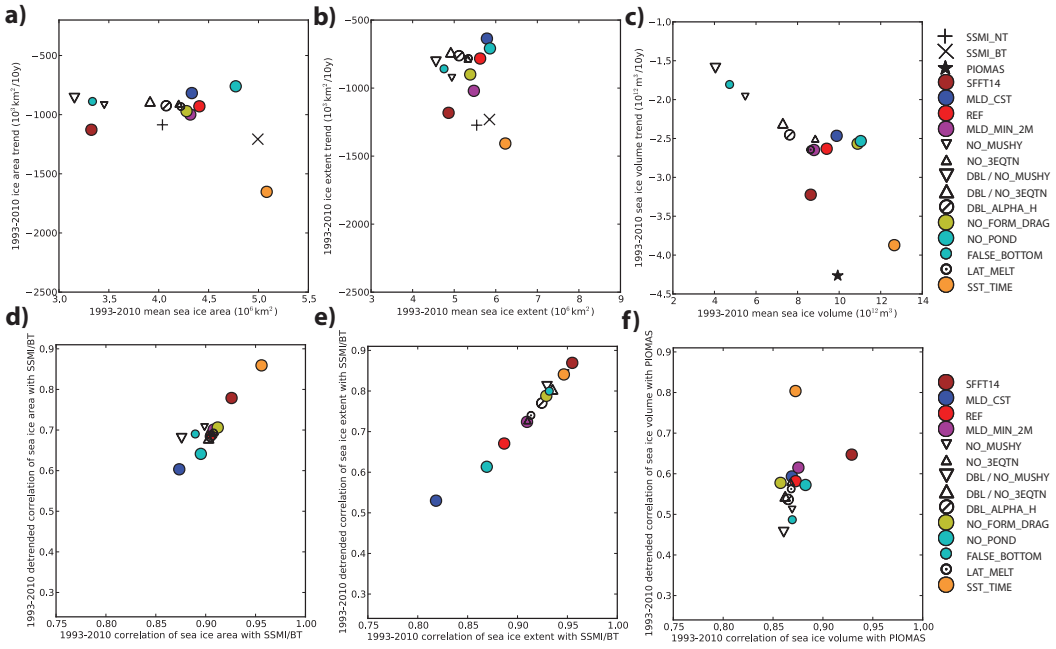

FIG. 14. Scatter plots of the trends vs averages over the period 1993 to 2010 of the September total sea ice area (a), sea ice extent (b) and sea ice volume (c). Scatter plots of the full and de-trended correlation coefficients between the model and observed time series of the total sea ice area (d), sea ice extent (e) and sea ice volume (f). Here we correlate model sea ice area and extent with the *SSMI_BT* observation and model volume with *PIOMAS*. We show 13 model runs described in section 2. As a reference we also show values from the model run discussed in Schröder et al. (2014).